



# Transient rod climbing in a viscoelastic fluid

Tachin Ruangkriengsin 10, Rodolfo Brandão 2,30, Katie Wu 10, Jonghyun Hwang, Evgeniy Boyko and Howard A. Stone to

Corresponding author: Howard A. Stone, hastone@princeton.edu

(Received 2 January 2025; revised 22 August 2025; accepted 27 August 2025)

The Weissenberg effect, or rod-climbing phenomenon, occurs in non-Newtonian fluids where the fluid interface ascends along a rotating rod. Despite its prominence, theoretical insights into this phenomenon remain limited. In earlier work, Joseph & Fosdick (1973, Arch. Rat. Mech. Anal. vol. 49, pp. 321–380) employed domain perturbation methods for second-order fluids to determine the equilibrium interface height by expanding solutions based on the rotation speed. In this work, we investigate the time-dependent interface height through asymptotic analysis with dimensionless variables and equations using the Giesekus model. We begin by neglecting inertia to focus on the interaction between gravity, viscoelasticity and surface tension. In the small-deformation scenario, the governing equations indicate the presence of a boundary layer in time, where the interface rises rapidly over a short time scale before gradually approaching a steady state. By employing a stretched time variable, we derive the transient velocity field and corresponding interface shape on this short time scale, and recover the steady-state shape on a longer time scale. In contrast to the work of Joseph and Fosdick, which used the method of successive approximations to determine the steady shape of the interface, we explicitly derive the interface shape for both steady and transient cases. Subsequently, we reintroduce small but finite inertial effects to investigate their interaction with viscoelasticity, and propose a criterion for determining the conditions under which rod climbing occurs. Through numerical computations, we obtain the transient interface shapes, highlighting the interplay between time-dependent viscoelastic and inertial effects.

**Key words:** rheology, viscoelasticity, polymers

<sup>&</sup>lt;sup>1</sup>Program in Applied and Computational Mathematics, Princeton University, Princeton, NJ 08544, USA

<sup>&</sup>lt;sup>2</sup>School of Mathematics, University of Bristol, Fry Building, Woodland Road, Bristol BS8 1UG, UK

<sup>&</sup>lt;sup>3</sup>Department of Mathematics, University of British Columbia, Vancouver, BC V6T 1Z2, Canada

<sup>&</sup>lt;sup>4</sup>Department of Mechanical and Aerospace Engineering, Princeton University, Princeton, NJ 08544, USA

<sup>&</sup>lt;sup>5</sup>Faculty of Mechanical Engineering, Technion – Israel Institute of Technology, Haifa 3200003, Israel

### 1. Introduction

The rod-climbing phenomenon, also known as the Weissenberg effect (Weissenberg 1947), is one of the most iconic examples of non-Newtonian fluid behaviour in which the fluid's surface climbs along a rotating rod. Heuristically, this effect arises from the interplay between elastic and viscous forces in complex fluids, where the unequal normal stresses within the fluid generate a hoop stress around the rod, driving an upward motion (Bird, Armstrong & Hassager 1987). Its visually compelling nature has made the rod-climbing phenomenon a foundational concept in the study of non-Newtonian fluid flows, serving as an essential tool in both pedagogical and research contexts (Ewoldt & Saengow 2022). Although it is widely recognised, theoretical insights into this phenomenon remain limited, owing to the challenges in modelling the constitutive equations for such fluids.

The earliest theoretical attempt to explain the rod-climbing phenomenon dates back to the work of Serrin (1959), who derived the unidirectional Couette flow solution for second-order fluids. By neglecting the non-equilibrated shear stress at the free surface, Serrin calculated the rise height and identified the conditions under which the fluid's free surface would climb the rod. A similar calculation, introduced by Giesekus (1961) two years after Serrin's work, neglects inertial effects but applies to a wider range of constitutive equations; however, the issue of non-equilibrated shear stress along the free surface remains unresolved. Both Serrin and Giesekus asserted that their solutions would remain valid, approximately, as long as the free surface remained relatively horizontal. Building on this concept of small deformations, Joseph & Fosdick (1973) developed a systematic framework for constructing the steady free-surface shape of second-order fluids using the domain perturbation method. This solution involved a perturbation series for both the flow profile and the fluid domain based on a prescribed (small) angular velocity  $\Omega$ . In subsequent works, Joseph, Beavers & Fosdick (1973) and Beavers, Yoo & Joseph (1980) compared their theoretical predictions with the experimental observations, finding good agreement. In fact, the theoretical work of Joseph & Fosdick (1973), completed over 50 years ago, continues to be widely used for rheological measurements today (More et al. 2023). Building on the pioneering work of Joseph & Fosdick (1973), several studies have extended the original framework using perturbative approaches. For example, Yoo, Joseph & Beavers (1979) developed a higher-order theory of the rod-climbing phenomenon by expanding the perturbation series to  $O(\Omega^4)$ . Meanwhile, Signer (1984) analysed the free surface of second-order fluids between vertical cylinders rotating about non-concentric axes, utilising the domain perturbation method and bipolar coordinates to aid the analysis.

Beyond its theoretical significance, the rod-climbing phenomenon has substantial practical applications in rheology. In particular, several studies highlighted its utility in rheometric applications to determine key material parameters, such as normal stress coefficients and relaxation times, by analysing climbing heights and rates (Beavers & Joseph 1975; Choi 1991; Choi & Kim 1992). More recently, More *et al.* (2023) revisited rod-climbing rheometry with the aid of a modern torsional rheometer. By integrating rod-climbing experiments with small-amplitude oscillatory shear flow measurements and steady-shear measurements from commercial rheometers, they successfully predicted the normal stress coefficients of a polymer solution at low shear rates, extending below the sensitivity range of conventional rheometers.

To date, all theoretical studies on the rod-climbing phenomenon have focused exclusively on its steady-state behaviour and have been limited to second-order fluid models. However, the use of second-order fluids comes with several limitations. First, the retarded-motion expansion (e.g. second-order and third-order fluid models) is valid only for small Deborah or Weissenberg numbers (Bird *et al.* 1987); applying it beyond this range

can lead to unphysical results. Second, second-order fluid models are highly unstable. For instance, a steady shear flow in a second-order fluid is unstable to short-wavelength perturbations, which, when combined with time-dependent flows, lead to local exponential growth in stress (Morozov & Spagnolie 2015). In this work, we focus on investigating the transient dynamics of the rod-climbing phenomenon. Access to a time-dependent shape enables a more accurate application of rod-climbing rheometry, providing a valuable tool for both advancing the theoretical understanding of the flows of non-Newtonian fluids and leveraging the results to determine material properties.

As noted above, second-order fluid models suffer from a lack of well-posedness in unsteady flows, making them unsuitable for modelling transient phenomena such as rod climbing. One popular model that offers a more robust alternative by enabling stable predictions in time-dependent settings is the Oldroyd-B model, which is used widely for characterising the behaviour of constant shear-viscosity viscoelastic fluids, such as Boger fluids (James 2009). The model also offers valuable physical intuition through its connection to the kinetic theory of dilute polymer solutions, where the polymer is represented as a dumbbell structure of two beads connected by a linear elastic spring. However, the Oldroyd-B model assumes constant shear viscosity and isotropic drag, which limits its ability to describe more complex viscoelastic fluids that exhibit nonlinear rheological behaviour.

In this work, we instead adopt the Giesekus model (Giesekus 1982), a constitutive equation for polymer solutions and melts that is able to predict several key features of complex fluids, such as non-zero second normal stress differences, shear thinning, and finite extensional viscosity (Giesekus 1982; Bird *et al.* 1987). The Giesekus model extends the Oldroyd-B framework by introducing a quadratic nonlinear anisotrotopic mobility term that reflects interactions among polymer chains (Giesekus 1982), thereby providing a more realistic representation of microstructural dynamics in complex viscoelastic fluids.

To conclude this section, we summarise in table 1 the previous theoretical works on flows near a rotating rod in complex fluids, with and without accounting for the free surface. The remaining sections of this paper are organised as follows. In § 2, we present the problem formulation, including the scalings for the variables and the governing equations. In § 3, we outline the preliminary set-up and introduce the techniques used in later sections, such as the distinguished limit of the problem, the perturbation expansion in Weissenberg number, and the domain perturbation method for simplifying the interface boundary conditions. In § 4, we exclude inertial effects and derive the steady interface shape that represents the long-time free-surface behaviour. In § 5, we extend the steady interface analysis by examining the short time scale to obtain the transient dynamics and the time-varying interface shapes. In § 6, we reintroduce small but finite inertial effects to explore the interplay between inertia and viscoelasticity, and examine the conditions under which the fluid climbs the rod. We conclude with a discussion of the results in § 7.

#### 2. Problem formulation

We investigate the rotation of an infinitely long rod with angular velocity  $\Omega$ , where the rod has radius a, and its axis is aligned along the z-direction, while immersed in a dilute viscoelastic polymer solution with density  $\rho$ . We assume that the flow is axisymmetric, and employ cylindrical coordinates  $(r, \theta, z)$  to examine the time-dependent free-surface shape h(r, t) of a viscoelastic fluid, with the reference height taken to be zero as  $r \to \infty$ , as shown in figure 1. Our analysis primarily focuses on the case where the interface deformation is considered 'small', i.e.  $|\partial h/\partial r| \ll 1$ , with the validity of this assumption to be clarified below through asymptotic analysis.

Model	Flow field		Rise height		Remarks	Reference
	Steady	Unsteady	Steady	Unsteady		
Second-order fluid	Yes	No	Yes*	No	*Partial calculations	Serrin (1959), Giesekus (1961)
	Yes	No	Yes	No	Include inertia and surface tension	Joseph & Fosdick (1973)
	Yes	No	Yes	No	Higher-order approximation	Yoo et al. (1979)
	Yes	No	Yes	No	Non-concentric cylinders	Siginer (1984)
Oldroyd-B	Yes	No	No	No	Obtained vertical normal stresses	Oldroyd (1950, 1951)
Giesekus	Yes	Yes	Yes	Yes		Current work

Table 1. Theoretical studies on flows around a vertically oriented rotating rod in complex fluids. The work of Joseph & Fosdick (1973) has been reproduced using modern notation by More *et al.* (2023).

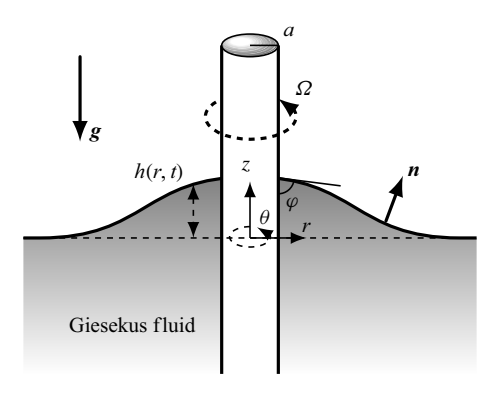


Figure 1. Schematic illustration of an infinite rod with radius a rotating with angular speed  $\Omega$  in a viscoelastic fluid.

To model the viscoelastic contributions to the rod-climbing effect, we employ the Giesekus constitutive equation (Giesekus 1982; Bird *et al.* 1987). In this model, the total stress tensor  $\sigma$  in the fluid can be expressed as

$$\boldsymbol{\sigma} = -p\boldsymbol{I} + 2\mu_s \boldsymbol{E} + \boldsymbol{\sigma}_p, \tag{2.1}$$

where the first term in (2.1) represents the pressure component, the second term in (2.1) denotes the viscous stress from the solvent with viscosity  $\mu_s$ , where  $\mathbf{E} = (1/2)(\nabla \mathbf{u} + (\nabla \mathbf{u})^T)$  is the rate-of-strain tensor, and the last term in (2.1) accounts for the polymeric contribution to the stress. As the polymer is suspended in the fluid, it experiences stretching, reorientation and advection, which, in the Giesekus model, results in the evolution of the polymeric stress according to

$$\boldsymbol{\sigma}_{p} + \lambda \left( \frac{\partial \boldsymbol{\sigma}_{p}}{\partial t} + \boldsymbol{u} \cdot \nabla \boldsymbol{\sigma}_{p} - \boldsymbol{\sigma}_{p} \cdot \nabla \boldsymbol{u} - (\nabla \boldsymbol{u})^{\mathrm{T}} \cdot \boldsymbol{\sigma}_{p} \right) + \frac{\alpha \lambda}{\mu_{p}} \boldsymbol{\sigma}_{p} \cdot \boldsymbol{\sigma}_{p} = 2\mu_{p} \boldsymbol{E}, \quad (2.2)$$

where u is the velocity vector,  $\lambda$  is the relaxation time of the polymer,  $\mu_p$  is the polymer viscosity at zero shear rate, and  $\alpha$  is the mobility factor, taking values between 0 and

1/2, which describes the anisotropic hydrodynamic drag on a polymer. When  $\alpha = 0$ , the Giesekus model reduces to the Oldroyd-B constitutive model (Oldroyd 1950; Bird *et al.* 1987).

In §§ 4 and 5, we will assume that the Reynolds number defined by

$$Re = \frac{\rho a^2 \Omega}{\mu_s + \mu_p} \tag{2.3}$$

is small, i.e.  $Re \ll 1$ . This assumption is valid, for instance, when the rod's angular rotation speed is low, in line with the assumption that the deformation along the free surface is small. Neglecting inertial effects, the continuity and momentum equations become

$$\nabla \cdot \boldsymbol{u} = 0$$
 and  $\nabla \cdot \boldsymbol{\sigma} = \rho g \boldsymbol{e}_{z}$ , (2.4)

where  $e_z$  is directed vertically upwards. We will revisit the role of small but finite inertial effects in § 6. Equations (2.1), (2.2) and (2.4) form the basis of the Giesekus constitutive description and model flow equations that we investigate in the upcoming sections.

These equations are supplemented with boundary and initial conditions applied to the rotating rod, the free surface, and the far-field region. First, we assume the no-slip boundary condition along the surface of the rotating rod,

$$\mathbf{u} = a\Omega \mathbf{e}_{\theta} \quad \text{at} \quad r = a,$$
 (2.5)

and the contact angle boundary condition

$$\frac{\partial h}{\partial r} = -\cot \varphi \quad \text{at} \quad r = a, \tag{2.6}$$

where  $\varphi$  is the contact angle of the fluid–air interface at the rotating rod. To simplify our analysis so that the interface shape can be derived analytically, we set  $\varphi = \pi/2$ , which results in  $\cot \varphi = 0$ . This corresponds to the case where no static capillary rise occurs near the rod's surface when the rod is at rest, eliminating any ambiguity in defining the initial condition of the interface shape. Quantitatively, our analysis provides a formula for the additional rise height beyond the static capillary rise height.

In the far field,  $r \to \infty$ , we assume that the interface remains flat, the fluid velocity decreases to zero, and the microstructure remains in its equilibrium state:

$$h \to 0$$
,  $u \to 0$ ,  $\sigma_p \to 0$  as  $r \to \infty$ . (2.7)

Next, we impose both the stress and kinematic boundary conditions along the free surface, z = h(r, t), which has unit outward normal n. The stress boundary condition along the interface, referencing the fluid pressure to the ambient pressure, is

$$\mathbf{n} \cdot \mathbf{\sigma} = -\gamma (\nabla_s \cdot \mathbf{n}) \mathbf{n}$$
 at  $z = h(r, t)$ , (2.8)

where  $\gamma$  denotes the surface tension, and  $\nabla_s$  is the surface gradient operator. On the other hand, the kinematic boundary condition along the interface is given by

$$\frac{\partial h}{\partial t} = u_z - u_r \frac{\partial h}{\partial r}$$
 at  $z = h(r, t)$ . (2.9)

Finally, we assume that the interface is flat and the polymer is in its equilibrium state at the initial time:

$$h = 0, \quad \sigma_p = 0 \quad \text{at} \quad t = 0.$$
 (2.10)

It is important to note that by making the low-Reynolds-number assumption, we have neglected the time derivative of the velocity field, which prevents us from specifying the velocity at the initial time.

# 2.1. Scalings and governing equations in dimensionless form

We now rescale all relevant variables. Specifically, we rescale lengths by a, velocities by  $a\Omega$ , stresses by  $(\mu_s + \mu_p)\Omega$ , and time by  $1/\Omega$ :

$$Z = \frac{z}{a}, \quad R = \frac{r}{a}, \quad H = \frac{h}{a}, \quad U = \frac{u}{a\Omega}, \quad T = t\Omega,$$

$$E = \frac{E}{\Omega}, \quad P = \frac{p}{(\mu_s + \mu_p)\Omega}, \quad \Sigma' = \frac{\sigma}{(\mu_s + \mu_p)\Omega}, \quad \Sigma_p = \frac{\sigma_p}{(\mu_s + \mu_p)\Omega}. \quad (2.11)$$

These dimensionless variables are accompanied by dimensionless parameters for viscosity ratios

$$\beta_p = \frac{\mu_p}{\mu_s + \mu_p} \quad \text{and} \quad \beta_s = 1 - \beta_p, \tag{2.12}$$

the Weissenberg number Wi, the gravity parameter  $\mathcal{G}$ , and the capillary number Ca:

$$Wi = \lambda \Omega, \quad \mathcal{G} = \frac{\rho g a}{(\mu_s + \mu_p)\Omega}, \quad Ca = \frac{(\mu_s + \mu_p)a\Omega}{\gamma}.$$
 (2.13)

The Weissenberg number Wi, defined as the product of the fluid's relaxation time and the characteristic shear rate, is commonly used to assess the viscoelastic properties of a material, indicating whether its behaviour is more elastic or more viscous. In experiments, Wi typically ranges from 1 to 10 or higher. In this work, however, we restrict attention to sufficiently small Wi, allowing us to employ a regular perturbation expansion in Wi. Although it is difficult to measure the interface height experimentally when Wi < 1, we anticipate that our analysis may provide insights applicable to larger Wi. Another key parameter is the Deborah number De, which represents the ratio of the material's response time to the characteristic time of the flow. In this problem, Wi and De are equivalent, so no distinction is made between the two. Here, we focus on the case where  $Wi \ll 1$ , corresponding to weak viscoelastic effects. The ranges of  $\mathcal{G}$  and Ca will depend on the value of Wi, so that we can derive analytical expressions for the small deformation of the interface shape H, as will be discussed in § 3.1.

Using the scalings in (2.11), the governing equations (2.1), (2.2) and (2.4) become

$$\nabla \cdot \boldsymbol{U} = 0, \quad \nabla \cdot \boldsymbol{\Sigma}' = \mathcal{G}\boldsymbol{e}_{z}, \tag{2.14a}$$

$$\Sigma' = -PI + 2\beta_s E + \Sigma_p, \qquad (2.14b)$$

$$\boldsymbol{\Sigma}_{p} + Wi\left(\frac{\partial \boldsymbol{\Sigma}_{p}}{\partial T} + \boldsymbol{U} \cdot \nabla \boldsymbol{\Sigma}_{p} - \boldsymbol{\Sigma}_{p} \cdot \nabla \boldsymbol{U} - (\nabla \boldsymbol{U})^{\mathrm{T}} \cdot \boldsymbol{\Sigma}_{p}\right) + \frac{\alpha Wi}{\beta_{p}} \boldsymbol{\Sigma}_{p} \cdot \boldsymbol{\Sigma}_{p} = 2\beta_{p} \boldsymbol{E}.$$
(2.14c)

Similarly, the corresponding boundary and initial conditions (2.5)–(2.10) become

No-slip boundary condition: 
$$U = e_{\theta}$$
 at  $R = 1$ , (2.15a)

Contact angle boundary condition: 
$$\frac{\partial H}{\partial R} = 0$$
 at  $R = 1$ , (2.15b)

Stress boundary condition: 
$$\mathbf{n} \cdot \mathbf{\Sigma}' = -\frac{1}{Ca} (\nabla_s \cdot \mathbf{n}) \mathbf{n}$$
 at  $Z = H(R, T)$ , (2.15c)

Kinematic boundary condition: 
$$\frac{\partial H}{\partial T} = U_z - U_r \frac{\partial H}{\partial R}$$
 at  $Z = H(R, T)$ , (2.15*d*)

Far field: 
$$H \to 0$$
,  $U \to \mathbf{0}$ ,  $\Sigma_p \to \mathbf{0}$  as  $R \to \infty$ , (2.15*e*)

Initial condition:  $H = 0$ ,  $\Sigma_p = \mathbf{0}$  at  $T = 0$ . (2.15*f*)

Initial condition: 
$$H = 0$$
,  $\Sigma_p = \mathbf{0}$  at  $T = 0$ . (2.15 $f$ )

To further simplify the momentum equation (2.14*a*), it is useful to introduce a modified pressure variable above hydrostatic pressure and redefine the stress tensor to incorporate the conservative gravitational force:

$$\Sigma = \Sigma' - \mathcal{G}ZI, \quad \mathcal{P} = P + \mathcal{G}Z.$$
 (2.16)

With these reformulated variables, the total stress equation in the fluid (2.14b) and the momentum equation (2.14a) simplify to

$$\Sigma = -\mathcal{P}I + 2\beta_s E + \Sigma_p, \quad \nabla \cdot \Sigma = 0. \tag{2.17}$$

To account for the new variables, the stress boundary condition (2.15c) becomes

$$\mathbf{n} \cdot \mathbf{\Sigma} = -\left(\mathcal{G}Z + \frac{1}{Ca}(\nabla_s \cdot \mathbf{n})\right)\mathbf{n}$$
 at  $Z = H(R, T)$ . (2.18)

# 3. Preliminary set-ups

# 3.1. Distinguished limit

We focus on three key non-dimensional parameters, i.e. the Weissenberg number Wi, the gravity parameter  $\mathcal{G}$ , and the capillary number Ca; we assume that the viscosity ratio  $\beta_p$  is given. It is natural to examine the asymptotic limit where  $Wi \ll 1$  in which viscoelasticity appears as a correction to the Newtonian flow. However, careful consideration of the ranges of  $\mathcal{G}$  and Ca is required, as different values of these parameters will lead to different asymptotic regimes depending on Wi. Before advancing our analysis, we will investigate how key quantities, e.g. velocity, pressure, polymeric stress and interface height, depend on these non-dimensional parameters, to gain insight into the distinguished limit that forms the foundation of our study.

First, we consider the relationship between the gravity parameter and the capillary number. A natural dimensionless quantity that characterises the ratio of gravitational to capillary forces is the Bond number, defined as

$$B = \frac{\rho g a^2}{\gamma} = Ca \mathcal{G}. \tag{3.1}$$

In the following sections, we aim to incorporate both effects into our analysis. To this end, we assume that the Bond number is of order unity, i.e. B = O(1). This allows us to write the capillary number in terms of the Bond number and the gravity parameter,  $Ca = B/\mathcal{G}$ .

Next, we consider the relationship between the Weissenberg number and the gravity parameter. Initially, we assume that the polymers are in equilibrium. As the rod begins rotating at a constant angular velocity, the fluid forms a vortex around the rod, causing the suspended polymers to stretch. Once the polymers extend beyond their equilibrium state, they induce additional polymeric stress of order O(Wi):

$$\Sigma_p \sim Wi.$$
 (3.2)

When viscoelasticity is absent from the flow, the Stokes flow only yields a flat interface, i.e. in the absence of inertial effects. Therefore, we expect the normal stress near the interface to arise from the polymeric stress. Using the normal stress boundary condition (2.18), we find that the normal stress near the interface (deformation H), in the limit of small deformation, behaves as

$$\Sigma \sim \Sigma_p \sim \mathcal{G}H$$
 (near the interface). (3.3)

Here, we have assumed that the gravitational and capillary effects are comparable when B = O(1). By combining (3.2) and (3.3), we anticipate that the typical interface height will depend on both viscoelasticity and gravity as

$$H \sim \frac{Wi}{\mathcal{G}}.$$
 (3.4)

As discussed earlier, the dynamics of the interface is driven by the (weak) viscoelasticity of the fluid. Therefore, we expect the characteristic time scale for temporal changes in the interface height to be determined by the polymer relaxation time, rather than the flow time scale itself. With this in mind, we use the kinematic boundary condition (2.15*d*) and the typical interface height (3.4) to estimate the typical magnitude of the upward fluid velocity near the interface as

$$U_{interface} \sim \frac{H}{Wi} \sim \frac{1}{\mathcal{C}}.$$
 (3.5)

Near the interface, we observe from (3.2) that the polymeric stress scales as Wi, whereas from (3.5), the viscous stress scales like  $\mathcal{G}^{-1}$ . When  $1 \gg Wi \gg \mathcal{G}^{-1}$ , the normal stress at the interface comes mainly from the polymeric stress, as we had assumed to obtain (3.3).

However, when  $\mathcal{G} = Wi^{-1}$ , the upward flow near the interface induces a viscous stress comparable to the polymeric stress, adding further complexity to the problem. The distinguished limit  $\mathcal{G} = Wi^{-1}$ , where our qualitative analysis (3.2)–(3.5) begins to break down, motivates us to explore the gravity parameter  $\mathcal{G}$  within the range  $\mathcal{G} \gtrsim Wi^{-1}$ . To simplify the complexity of the double asymptotic expansion into a single expansion in terms of Wi, based on the distinguished limit  $\mathcal{G} = Wi^{-1}$ , we introduce a rescaled gravity parameter G by defining

$$G = Wi\mathcal{G},\tag{3.6}$$

where G is now taken to be of order O(1). Intuitively, when gravitational effects are large  $(G \gg 1)$ , the viscoelastic fluid has difficulty climbing the rotating rod, which leads to only small deformations on the interface shape. This is precisely the small-deformation situation that we aim to address in this study.

### 3.2. Perturbation expansion in Weissenberg number

In the following sections, we expand the velocity, pressure and the polymeric stress as regular perturbations in  $Wi \ll 1$ ,

$$\mathcal{P} = \mathcal{P}^{(0)} + Wi\mathcal{P}^{(1)} + \cdots, \qquad (3.7a)$$

$$E = E^{(0)} + WiE^{(1)} + \cdots,$$
 (3.7b)

$$\Sigma_p = \Sigma_p^{(0)} + Wi\Sigma_p^{(1)} + \cdots, \qquad (3.7c)$$

where the superscript indicates the corresponding order in Wi. Along with the quantities expressed as expansions in (3.7), we introduce an expansion of the interface shape in the situation where the interface is slightly deformed:

$$H(R, T) = Wi^2 H^{(2)} + Wi^3 H^{(3)} + \cdots$$
 (3.8)

Although it is more natural to start the expansion of H at order O(Wi), since the interface remains flat in the absence of viscoelasticity, we have opted to express it as in (3.8) for two reasons. First, we observe from our preliminary scaling argument (3.4) that  $H \sim Wi\mathcal{G}^{-1} \sim Wi^2 G^{-1} = O(Wi^2)$ . Second, as we will see in § 3.3, expanding the free-surface boundary condition to be consistent with the perturbation expansion in the

Weissenberg number involves extensive calculations unless each term is scaled correctly. By keeping the non-zero leading-order expansion of H, the derivations for the boundary conditions at each order become more organised. In this work, we focus on obtaining an analytical formula for the leading-order term of the interface shape  $H^{(2)}$ , given in (3.8).

# 3.3. Domain perturbation method for the interface boundary condition

In § 2.1, we introduced the normal stress boundary condition (2.18) and the kinematic boundary condition (2.15d), in which both boundary conditions are evaluated at the interface Z = H. However, when expanding the interface shape H in terms of Wi (see (3.8)), it is challenging to evaluate the boundary conditions using the full series expansion. To resolve this issue, we take advantage of the assumption that the interface deformation is small to simplify the boundary conditions using a domain perturbation expansion. This step enables us to systematically write down the corresponding interface boundary conditions for the velocity, pressure and polymeric stress fields at each order in Wi.

We start by expressing the normal stress boundary condition (2.18) at each order in Wi. The assumption of small deformation of the interface provides two simplifications. First, we can approximate the normal vector  $\mathbf{n}$  at the interface as  $\mathbf{n} \approx \mathbf{e}_z - (\partial H/\partial R)\mathbf{e}_r = \mathbf{e}_z + O(Wi^2)\mathbf{e}_r$ . Second, when evaluating the boundary condition at Z = H, the small value of H allows us to perform a Taylor expansion around Z = 0. From these two remarks, we may simplify the left-hand side of (2.18) as

$$|\mathbf{n} \cdot \mathbf{\Sigma}|_{Z=H} = \mathbf{n} \cdot \mathbf{\Sigma} \Big|_{Z=0} + H \frac{\partial (\mathbf{n} \cdot \mathbf{\Sigma})}{\partial Z} \Big|_{Z=0} + \frac{1}{2} H^2 \frac{\partial^2 (\mathbf{n} \cdot \mathbf{\Sigma})}{\partial Z^2} \Big|_{Z=0} + \cdots$$

$$= \mathbf{e}_z \cdot \left( -\mathcal{P}^{(0)} \mathbf{I} + 2\beta_s \mathbf{E}^{(0)} + \mathbf{\Sigma}_p^{(0)} \right) \Big|_{Z=0}$$

$$+ Wi \left( \mathbf{e}_z \cdot \left( -\mathcal{P}^{(1)} \mathbf{I} + 2\beta_s \mathbf{E}^{(1)} + \mathbf{\Sigma}_p^{(1)} \right) \Big|_{Z=0} \right) + O(Wi^2). \tag{3.9}$$

On the other hand, the small-deformation assumption allows us to simplify the curvature of the interface  $(\nabla_s \cdot \mathbf{n})$  so that the right-hand side of (2.18) becomes

$$-\left(\mathcal{G}Z + \frac{1}{Ca}(\nabla_{s} \cdot \boldsymbol{n})\right)\boldsymbol{n}\Big|_{Z=H} = -\left(\mathcal{G}H - \frac{1}{Ca}\frac{1}{R}\frac{\partial}{\partial R}\left(R\frac{\partial H}{\partial R}\right)\right)\boldsymbol{e}_{z} + O(Wi^{2})$$

$$= -WiG\left(H^{(2)} - \frac{1}{BR}\frac{\partial}{\partial R}\left(R\frac{\partial H^{(2)}}{\partial R}\right)\right)\boldsymbol{e}_{z} + O(Wi^{2}).$$
(3.10)

Combining (3.9) and (3.10), we conclude that the stress boundary condition (2.18) at O(1) and O(Wi) becomes

$$\mathbf{e}_z \cdot \left. \left( -\mathcal{P}^{(0)} \mathbf{I} + 2\beta_s \mathbf{E}^{(0)} + \mathbf{\Sigma}_p^{(0)} \right) \right|_{Z=0} = \mathbf{0}, \tag{3.11a}$$

$$\mathbf{e}_{z} \cdot \left. \left( -\mathcal{P}^{(1)} \mathbf{I} + 2\beta_{s} \mathbf{E}^{(1)} + \mathbf{\Sigma}_{p}^{(1)} \right) \right|_{Z=0} = -G \left( H^{(2)} - \frac{1}{BR} \frac{\partial}{\partial R} \left( R \frac{\partial H^{(2)}}{\partial R} \right) \right) \mathbf{e}_{z}. \quad (3.11b)$$

At this stage, we choose not to express the kinematic boundary condition (2.15d) for each order in Wi. As mentioned in § 3.1, the temporal evolution of the interface height is expected to be governed by the polymer relaxation time, rather than the flow time scale. This implies that, starting from a flat interface, the interface will rise rapidly

on a time scale of order O(Wi) before approaching its steady state. This behaviour suggests a boundary-layer-like structure in time, prompting the examination of two time scales: T = O(1) and T = O(Wi). In § 4, we focus on T = O(1), representing the outer layer approximation, to recover the steady-state interface shape. In § 5, we analyse the shorter time scale T = O(Wi) using a stretched time variable, corresponding to the inner layer approximation, to study the transient interface shape. We will revisit the kinematic boundary condition (2.15d) separately for each rescaled time in §§ 4 and 5.

# 4. Outer layer: the steady-state interface shape

### 4.1. Leading-order solution

In this subsection, we examine the interface dynamics for T=O(1), representing the state when time has progressed beyond the initial start-up of the flow. To this point, we have provided only a general qualitative outline explaining why a distinction in time scales is necessary. Now we examine the evolution of the polymeric stress by writing (2.14c) in non-dimensional form as

$$Wi\left(\frac{\partial \boldsymbol{\Sigma}_{p}}{\partial T} + \boldsymbol{U} \cdot \nabla \boldsymbol{\Sigma}_{p} - \boldsymbol{\Sigma}_{p} \cdot \nabla \boldsymbol{U} - (\nabla \boldsymbol{U})^{\mathrm{T}} \cdot \boldsymbol{\Sigma}_{p} + \frac{\alpha}{\beta_{p}} \boldsymbol{\Sigma}_{p} \cdot \boldsymbol{\Sigma}_{p}\right) = -\boldsymbol{\Sigma}_{p} + 2\beta_{p} \boldsymbol{E}.$$
(4.1)

Equation (4.1) features a first-order time derivative, with the highest-order term  $\partial \Sigma_p/\partial T$  being multiplied by a small parameter Wi. This structure frequently arises in boundary layer problems, where singular perturbation analysis is required to understand the solution behaviour. Typically, the analysis is split into two regions, one where (4.1) is used as is, and another where time is rescaled to maintain the dominance of the highest-order term; in this subsection, we focus on the former case.

Before proceeding further, we note that using (3.7), the right-hand side of (4.1) enables us to express the leading-order polymeric stress in terms of the leading-order velocity field:

$$\Sigma_p^{(0)} = 2\beta_p E^{(0)}. (4.2)$$

In addition, when T = O(1) and  $H = O(Wi^2)$ , we can derive the kinematic boundary conditions (2.15*d*) up to first-order terms, by employing a domain perturbation technique similar to that used in § 3.3, as

$$U_Z^{(0)}\Big|_{Z=0} = U_Z^{(1)}\Big|_{Z=0} = 0.$$
 (4.3)

To proceed with the problem solution, we substitute the leading-order polymeric stress (4.2) into the leading-order momentum equation (2.17) to obtain

$$\mathbf{0} = \nabla \cdot \left( -\mathcal{P}^{(0)} \mathbf{I} + 2\beta_s \mathbf{E}^{(0)} + \Sigma_p^{(0)} \right) = -\nabla \mathcal{P}^{(0)} + \nabla^2 \mathbf{U}^{(0)}, \tag{4.4}$$

where  $\beta_s + \beta_p = 1$ , and from (4.2), we have  $\nabla \cdot \Sigma_p^{(0)} = \beta_p \nabla^2 U^{(0)}$ . Further, substituting (4.2) into the leading-order stress boundary condition (3.11*a*) yields

$$\boldsymbol{e}_z \cdot \left( -\mathcal{P}^{(0)} \boldsymbol{I} + 2\boldsymbol{E}^{(0)} \right) \Big|_{Z=0} = \boldsymbol{0}. \tag{4.5}$$

The leading-order governing equation (4.4) is solved subject to the boundary conditions (2.15a), (2.15e), (4.3) and (4.5), which no longer depend on the viscoelastic effects. At this order, the problem simplifies to the rotation of a rod in a Newtonian fluid at low Reynolds number, which is known to produce an azimuthal vortex flow profile

described by

$$U^{(0)} = \frac{1}{R} e_{\theta}, \quad \mathcal{P}^{(0)} = 0.$$
 (4.6)

With this leading-order velocity profile, and (4.2), we can write down the leading-order polymeric stress:

$$\Sigma_p^{(0)} = 2\beta_p E^{(0)} = -\frac{2\beta_p}{R^2} (e_r e_\theta + e_\theta e_r). \tag{4.7}$$

Notice that (4.7) does not satisfy the condition  $\Sigma_p^{(0)} = \mathbf{0}$  at the initial time; we will resolve this point in § 5.

### 4.2. First-order correction to the solution

We now proceed to determine the first-order correction to the shape of the interface. From (4.7), we observe that the leading-order polymeric stress appears as the rate-of-strain tensor from the leading-order vortical flow. This tensor has zero diagonal elements, resulting in no normal stress differences, which are typically responsible for the rod-climbing effect. To reveal the 'hoop stress' that leads to the rod-climbing effect, we solve for the first-order correction to the polymeric stress. Considering again the evolution of the polymeric stress equation (4.1), and using (4.6) and (4.7), we obtain

$$\boldsymbol{\Sigma}_{p}^{(1)} = -\boldsymbol{U}^{(0)} \cdot \boldsymbol{\nabla} \boldsymbol{\Sigma}_{p}^{(0)} + \boldsymbol{\Sigma}_{p}^{(0)} \cdot \boldsymbol{\nabla} \boldsymbol{U}^{(0)} + (\boldsymbol{\nabla} \boldsymbol{U}^{(0)})^{\mathrm{T}} \cdot \boldsymbol{\Sigma}_{p}^{(0)} - \frac{\alpha}{\beta_{p}} \boldsymbol{\Sigma}_{p}^{(0)} \cdot \boldsymbol{\Sigma}_{p}^{(0)} + 2\beta_{p} \boldsymbol{E}^{(1)}$$

$$= -\frac{4\beta_{p}}{R^{4}} (\boldsymbol{e}_{r} \boldsymbol{e}_{r} - \boldsymbol{e}_{\theta} \boldsymbol{e}_{\theta}) + \frac{4\beta_{p}}{R^{4}} (\boldsymbol{e}_{r} \boldsymbol{e}_{r} + \boldsymbol{e}_{\theta} \boldsymbol{e}_{\theta}) - \frac{4\beta_{p} \alpha}{R^{4}} (\boldsymbol{e}_{r} \boldsymbol{e}_{r} + \boldsymbol{e}_{\theta} \boldsymbol{e}_{\theta}) + 2\beta_{p} \boldsymbol{E}^{(1)}$$

$$= \frac{4\beta_{p}}{R^{4}} ((2 - \alpha)\boldsymbol{e}_{\theta} \boldsymbol{e}_{\theta} - \alpha \boldsymbol{e}_{r} \boldsymbol{e}_{r}) + 2\beta_{p} \boldsymbol{E}^{(1)}.$$
(4.8)

As in § 4.1, we substitute (4.8) into the momentum equation (2.17) at first order, to find

$$\mathbf{0} = -\nabla \mathcal{P}^{(1)} + \beta_s \, \nabla^2 \mathbf{U}^{(1)} + \nabla \cdot \mathbf{\Sigma}_p^{(1)}$$

$$= -\nabla \mathcal{P}^{(1)} + \nabla^2 \mathbf{U}^{(1)} + 4\beta_p \, \nabla \cdot \left(\frac{2-\alpha}{R^4} \mathbf{e}_{\theta} \mathbf{e}_{\theta} - \frac{\alpha}{R^4} \mathbf{e}_r \mathbf{e}_r\right)$$

$$= -\nabla \mathcal{P}^{(1)} + \nabla^2 \mathbf{U}^{(1)} - \frac{8\beta_p (1-2\alpha)}{R^5} \mathbf{e}_r. \tag{4.9}$$

Although the anisotropic hydrodynamic drag in the Giesekus model contributes to both shear-thinning behaviour and a non-zero second normal stress difference, we observe from (4.8) and (4.9) that only the normal stress is responsible for the rod climbing at this order. In particular, the second normal stress difference, represented by the terms containing the mobility factor  $\alpha$ , decreases the magnitude of the hoop stress in the final term of (4.9), thereby reducing the rise height, while the shear-thinning behaviour of the Giesekus fluid affects the interface shape at higher-order corrections.

Observe from (4.8) that  $\mathbf{e}_z \cdot \mathbf{\Sigma}_p^{(1)} = 2\beta_p \mathbf{e}_z \cdot \mathbf{E}^{(1)}$ . Thus we can rewrite the stress boundary condition (3.11b) at first order in Wi as

$$\boldsymbol{e}_{z} \cdot \left( -\mathcal{P}^{(1)} \boldsymbol{I} + 2\boldsymbol{E}^{(1)} \right) \Big|_{Z=0} = -G \left( H^{(2)} - \frac{1}{BR} \frac{\mathrm{d}}{\mathrm{d}R} \left( R \frac{\mathrm{d}H^{(2)}}{\mathrm{d}R} \right) \right) \boldsymbol{e}_{z}. \tag{4.10}$$

An important observation in solving the problem at first order is that all boundary conditions for the velocity field are constrained to be zero. Specifically,

the no-slip boundary condition (2.15a) imposes  $U^{(1)} = 0$  at R = 1, the far-field boundary condition (2.15e) enforces  $U^{(1)} = 0$  as  $R \to \infty$ , and the kinematic boundary condition (4.3) gives  $U_Z^{(1)}\big|_{Z=0} = 0$ . These features suggest  $U^{(1)} = 0$ , reducing the problem to solving for the pressure and interface height using (4.9) and (4.10) with the corresponding boundary conditions. Specifically, (4.9) implies that  $\mathcal{P}^{(1)}(R)$ , allowing us to simplify (4.10) to  $\mathcal{P}^{(1)} = G(H^{(2)} - (1/BR)(d/dR)(R dH^{(2)}/dR))$ . The far-field boundary condition (2.15e) then implies that the pressure decays to zero as the interface flattens, i.e.  $\mathcal{P}^{(1)}(R \to \infty) = 0$ .

We can now integrate the momentum equation (4.9) once with respect to R to find the pressure:

$$\mathcal{P}^{(1)}(R) = \frac{2\beta_p(1 - 2\alpha)}{R^4}. (4.11)$$

On the other hand, the free-surface shape  $H^{(2)}$  is governed by the differential equation

$$H^{(2)} - \frac{1}{BR} \frac{d}{dR} \left( R \frac{dH^{(2)}}{dR} \right) = \frac{2\beta_p (1 - 2\alpha)}{GR^4}.$$
 (4.12)

Equation (4.12) is subject to the contact angle boundary condition (2.15b) and the far-field condition (2.15e), yielding the solution

$$H_{steady}^{(2)}(R) = \frac{2\beta_{p}(1-2\alpha)B}{G} \left( I_{1}(\sqrt{B})K_{1}^{-1}(\sqrt{B}) \left( \int_{1}^{\infty} s^{-3}K_{0}(\sqrt{B}s) ds \right) K_{0}(\sqrt{B}R) + I_{0}(\sqrt{B}R) \int_{R}^{\infty} s^{-3}K_{0}(\sqrt{B}s) ds + K_{0}(\sqrt{B}R) \int_{1}^{R} s^{-3}I_{0}(\sqrt{B}s) ds \right),$$
(4.13)

where  $I_{\nu}$  and  $K_{\nu}$  are the first- and second-kind modified Bessel functions of order  $\nu$ , respectively. In figure 2, we present the scaled steady interface shape  $H(R) \mathcal{G}/[2\beta_p(1-2\alpha)Wi]$  around an infinitely long rotating rod in a Giesekus fluid for different Bond numbers.

Although it is not straightforward to visualise the height profile in (4.13), we can infer from (4.12) that for  $R \gg 1$ , the dominant balance is between the gravitational term and the viscoelastic term:

$$H_{steady}(R) \approx \frac{2\beta_p (1 - 2\alpha) Wi}{\mathcal{G}R^4} \quad (R \gg 1).$$
 (4.14)

A result similar to (4.14) was obtained previously for the second-order fluid model (Joseph & Fosdick 1973; More *et al.* 2023), which is known to agree with the Giesekus model at steady state for small Weissenberg numbers with  $\alpha = 0$ . However, in earlier studies, domain perturbation methods were developed using dimensional rotation speeds, without explicitly addressing the impact of individual dimensionless parameters. In addition, instead of providing solutions in explicit form, a method of successive approximations was used to estimate the final steady interface height. In §§ 5 and 6, we increase the complexity by introducing time-dependent and inertia terms, while maintaining the same dimensionless analytical structure established here.

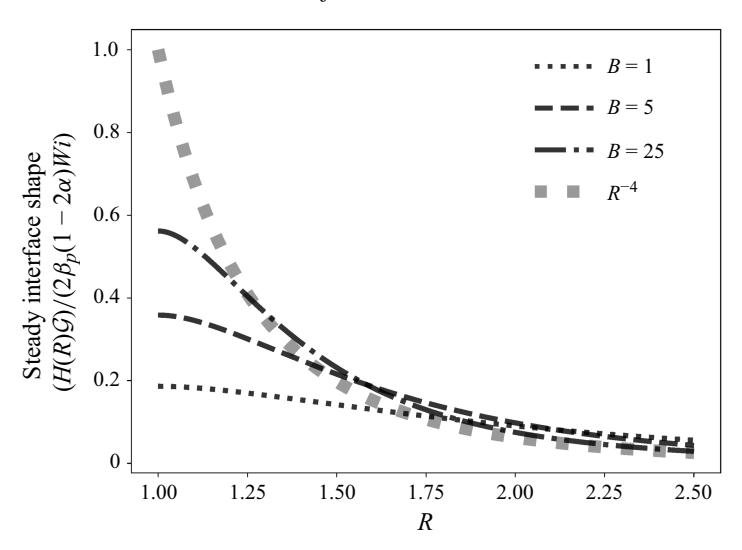


Figure 2. Steady interface shape around an infinitely long rotating rod in a Giesekus fluid, with inertial effects absent, displayed for different Bond numbers B = 1, 5, 25.

### 5. Inner layer: the transient interface shape

# 5.1. Leading-order solution

In § 4, we examined the problem at an intermediate time scale T=O(1), and observed that the leading-order interface shape (4.13) is time-independent. This result occurs because at T=O(1), substituting the polymeric stress expansion (3.7c) into (4.1) has corrections (4.7) and (4.8) that do not satisfy the initial condition  $\Sigma_p=0$  at T=0. Physically, these features suggest that no transient changes in the polymeric stress are observed at intermediate times, as the dynamics of these changes occurs on a much shorter time scale. Therefore, we introduce a stretched time variable to balance the time derivative term on the left-hand side of (4.1),  $Wi(\partial \Sigma_p/\partial T)$ , with the right-hand side of (4.1),  $-\Sigma_p + 2\beta_p E$ , by defining

$$\tau = \frac{T}{Wi}. ag{5.1}$$

In terms of physical variables, time has now been scaled by the relaxation time. More precisely, we rescale time by interpreting T = O(Wi) as  $\tau = O(1)$ .

The evolution equation for the polymeric stress (4.1) in terms of the stretched time variable  $\tau$  now becomes

$$Wi\left(\boldsymbol{U}\cdot\boldsymbol{\nabla}\boldsymbol{\Sigma}_{p}-\boldsymbol{\Sigma}_{p}\cdot\boldsymbol{\nabla}\boldsymbol{U}-(\boldsymbol{\nabla}\boldsymbol{U})^{\mathrm{T}}\cdot\boldsymbol{\Sigma}_{p}+\frac{\alpha}{\beta_{p}}\boldsymbol{\Sigma}_{p}\cdot\boldsymbol{\Sigma}_{p}\right)=-\left(\frac{\partial\boldsymbol{\Sigma}_{p}}{\partial\tau}+\boldsymbol{\Sigma}_{p}-2\beta_{p}\boldsymbol{E}\right),\tag{5.2}$$

where we distinguish the polymeric stress in the inner layer with  $\Sigma_p(R, Z, \tau)$ .

Following the approach in  $\S 4.1$ , we express the leading-order polymeric stress in terms of the leading-order velocity profile using (5.2) as

$$\frac{\partial \boldsymbol{\Sigma}_{p}^{(0)}}{\partial \tau} + \boldsymbol{\Sigma}_{p}^{(0)} = 2\beta_{p} \boldsymbol{E}^{(0)} \implies \boldsymbol{\Sigma}_{p}^{(0)} = 2\beta_{p} e^{-\tau} \int_{0}^{\tau} \boldsymbol{E}^{(0)} e^{s} ds, \qquad (5.3)$$

where we have used the condition  $\Sigma_p^{(0)} = \mathbf{0}$  at  $\tau = 0$ . We then substitute (5.3) into the leading-order momentum equation (2.17) to arrive at

$$\mathbf{0} = -\nabla \mathcal{P}^{(0)} + \beta_s \, \nabla^2 \mathbf{U}^{(0)} + \beta_p \, e^{-\tau} \int_0^{\tau} \nabla^2 \mathbf{U}^{(0)} \, e^s \, ds.$$
 (5.4)

Equation (5.4) is solved subject to the no-slip boundary condition (2.15a), the far-field boundary condition (2.15e), the stress boundary condition (3.11a), and the kinematic boundary condition (2.15d).

It is helpful to introduce a linear operator acting on the time-dependent vector field that resembles the right-hand side of (5.4) by defining

$$\mathcal{L}(\boldsymbol{F}(\boldsymbol{X},\tau)) = \beta_s \, \boldsymbol{F}(\boldsymbol{X},\tau) + \beta_p \, \mathrm{e}^{-\tau} \int_0^\tau \boldsymbol{F}(\boldsymbol{X},s) \, \mathrm{e}^s \, \mathrm{d}s, \tag{5.5}$$

so that (5.4) becomes  $\mathbf{0} = -\nabla \mathcal{P}^{(0)} + \mathcal{L}(\nabla^2 \mathbf{U}^{(0)})$ . With this notation, we simplify the stress boundary condition (3.11*a*) by substituting (5.3) to obtain

$$2\mathcal{L}\left(\boldsymbol{e}_{z}\cdot\boldsymbol{E}^{(0)}\Big|_{Z=0}\right) = \mathcal{P}^{(0)}\Big|_{Z=0}\boldsymbol{e}_{z}.$$
(5.6)

The kinematic boundary condition (2.15d), however, requires more careful examination, as it involves a time derivative that is crucial to the analysis in this section. Nevertheless, at leading order, we still find  $U_Z^{(0)}\big|_{Z=0}=0$ . Since the flow begins at rest with a flat interface, this absence of upward velocity suggests that the interface will remain flat throughout. Therefore, we aim to find a solution where  $U_Z^{(0)}$  is identically zero, and the velocity field  $U^{(0)}=U^{(0)}(R,\tau)$  is independent of Z. The continuity equation (2.14a), expressed in cylindrical coordinates as  $(1/R)(\partial(RU_R^{(0)})/\partial R)+(\partial U_Z^{(0)}/\partial Z)=0$ , then forces  $U_R^{(0)}=c(\tau)/R$  for some function  $c=c(\tau)$ . Applying the no-slip boundary condition (2.15a) implies  $c(\tau)=0$ , resulting in a purely azimuthal velocity field,  $U^{(0)}=U_Q^{(0)}(R,\tau)$   $e_\theta$ .

implies  $c(\tau)=0$ , resulting in a purely azimuthal velocity field,  $\boldsymbol{U}^{(0)}=U_{\theta}^{(0)}(R,\tau)\,\boldsymbol{e}_{\theta}$ . Continuing this approach, the momentum equation (2.17), at leading order in the r-and z-directions, yields  $\partial \mathcal{P}^{(0)}/\partial R=\partial \mathcal{P}^{(0)}/\partial Z=0$ , so that  $\mathcal{P}^{(0)}(\tau)$  only, while the stress boundary condition (5.6) in the z-direction further implies  $\mathcal{P}^{(0)}\equiv 0$ . Thus under the flat interface assumption, we have deduced that the pressure is absent from the leading-order solution. The momentum equation (2.17) and the stress boundary condition (5.6) simplify to

$$\mathcal{L}\left(\nabla^{2}\boldsymbol{U}^{(0)}\right) = \mathcal{L}\left(\boldsymbol{e}_{z} \cdot \boldsymbol{E}^{(0)} \Big|_{Z=0}\right) = \mathbf{0} \quad \Longrightarrow \quad \nabla^{2}\boldsymbol{U}^{(0)} = \boldsymbol{e}_{z} \cdot \boldsymbol{E}^{(0)} \Big|_{Z=0} = \mathbf{0}, \quad (5.7)$$

where we have used the fact that the kernel of the linear operator  $\mathcal{L}$  is null (see Appendix A).

We observe that (5.7) has the same structure as the leading-order solution analysed in § 4.1; in the weak viscoelastic limit, the leading-order solution is effectively Newtonian. Although the momentum equation (5.4) contains a time-dependent integral, the solution remains time-independent. Specifically, the velocity field retains the form of a vortex solution as in (4.6):

$$\boldsymbol{U}^{(0)} = \frac{1}{R} \boldsymbol{e}_{\theta}. \tag{5.8}$$

With this leading-order velocity profile, we can express the leading-order polymeric stress, using (5.3), as

$$\Sigma_p^{(0)} = 2\beta_p e^{-\tau} \int_0^{\tau} \mathbf{E}^{(0)} e^{s} ds = 2\beta_p (1 - e^{-\tau}) \mathbf{E}^{(0)} = -\frac{2\beta_p (1 - e^{-\tau})}{R^2} (\mathbf{e}_r \mathbf{e}_\theta + \mathbf{e}_\theta \mathbf{e}_r).$$
(5.9)

Starting from zero at  $\tau = 0$ ,  $\Sigma_p^{(0)}$  increases monotonically towards the steady state (4.7), approaching it with an exponential decay rate on the time scale of  $\tau$ . This behaviour confirms our remark at the start of this subsection that transient changes in the polymeric stress occur on a shorter time scale when T = O(Wi).

### 5.2. First-order correction solution

Hitherto, we have derived that for an inner layer in time where T = O(Wi), the leading-order flow remains the same vortex solution as in the outer layer over times T = O(1). Although the velocity fields are the same at the leading order, the leading-order polymeric stresses differ: in the inner layer,  $\Sigma_p^{(0)}$  varies with time, whereas it does not in the outer layer. Similarly, we anticipate the polymeric stress arising from  $\Sigma_p^{(1)}$ , which defined the interface shape in § 4.2, to also be time-dependent, enabling us to capture the transient interface shape. We can determine the time evolution of  $\Sigma_p^{(1)}$  using calculations similar to those in (4.8):

$$\frac{\partial \boldsymbol{\Sigma}_{p}^{(1)}}{\partial \tau} + \boldsymbol{\Sigma}_{p}^{(1)} = -\boldsymbol{U}^{(0)} \cdot \nabla \boldsymbol{\Sigma}_{p}^{(0)} + \boldsymbol{\Sigma}_{p}^{(0)} \cdot \nabla \boldsymbol{U}^{(0)} + (\nabla \boldsymbol{U}^{(0)})^{\mathrm{T}} \cdot \boldsymbol{\Sigma}_{p}^{(0)} 
- \frac{\alpha}{\beta_{p}} \boldsymbol{\Sigma}_{p}^{(0)} \cdot \boldsymbol{\Sigma}_{p}^{(0)} + 2\beta_{p} \boldsymbol{E}^{(1)} 
= -\frac{4\beta_{p}(1 - \mathrm{e}^{-\tau})}{R^{4}} (\boldsymbol{e}_{r} \boldsymbol{e}_{r} - \boldsymbol{e}_{\theta} \boldsymbol{e}_{\theta}) + \frac{4\beta_{p}(1 - \mathrm{e}^{-\tau})}{R^{4}} (\boldsymbol{e}_{r} \boldsymbol{e}_{r} + \boldsymbol{e}_{\theta} \boldsymbol{e}_{\theta}) 
- \frac{4\beta_{p}\alpha(1 - \mathrm{e}^{-\tau})^{2}}{R^{4}} (\boldsymbol{e}_{r} \boldsymbol{e}_{r} + \boldsymbol{e}_{\theta} \boldsymbol{e}_{\theta}) + 2\beta_{p} \boldsymbol{E}^{(1)} 
= \frac{4\beta_{p}}{R^{4}} ((2(1 - \mathrm{e}^{-\tau}) - \alpha(1 - \mathrm{e}^{-\tau})^{2}) \boldsymbol{e}_{\theta} \boldsymbol{e}_{\theta} - \alpha(1 - \mathrm{e}^{-\tau})^{2} \boldsymbol{e}_{r} \boldsymbol{e}_{r}) + 2\beta_{p} \boldsymbol{E}^{(1)}.$$
(5.10)

Multiplying both sides by the integrating factor  $e^{\tau}$ , we find  $\Sigma_p^{(1)}$  to be

$$\Sigma_{p}^{(1)} = 2\beta_{p} e^{-\tau} \int_{0}^{\tau} E^{(1)} e^{s} ds + \frac{4\beta_{p} \left(2 - \alpha - 2 e^{-\tau} - (2 - 2\alpha)\tau e^{-\tau} + \alpha e^{-2\tau}\right)}{R^{4}} e_{\theta} e_{\theta}$$
$$- \frac{4\beta_{p} \alpha \left(1 - 2\tau e^{-\tau} - e^{-2\tau}\right)}{R^{4}} e_{r} e_{r}, \tag{5.11}$$

where we have used the initial condition  $\Sigma_p^{(1)} = \mathbf{0}$  at  $\tau = 0$  to write the lower limit of the integral. We then substitute (5.11) into the first-order momentum equation (2.17) to obtain

$$\mathbf{0} = -\nabla \mathcal{P}^{(1)} + \beta_s \, \nabla^2 \mathbf{U}^{(1)} + \nabla \cdot \mathbf{\Sigma}_p^{(1)}$$

$$= -\nabla \mathcal{P}^{(1)} + \mathcal{L}(\nabla^2 \mathbf{U}^{(1)}) - \frac{8\beta_p \left(1 - 2\alpha - e^{-\tau} - (1 - 4\alpha)\tau e^{-\tau} + 2\alpha e^{-2\tau}\right)}{R^5} \mathbf{e}_r. \quad (5.12)$$

From (5.12), we observe that as the suspended polymers begin to stretch from their relaxed state, the elastic response generates a time-dependent force per volume that acts purely in the radial direction and is zero initially. This hoop stress is expected to drive the fluid radially inwards towards the rod, which then, by conservation of mass, would lead the interface to rise, resulting in the rod-climbing effect. Notably, the force induced by the hoop stress is conservative. Thus it is convenient to define a new pressure variable that includes the polymeric stress, by setting

$$P^{(1)} = \mathcal{P}^{(1)} - \frac{2\beta_p \left(1 - 2\alpha - e^{-\tau} - (1 - 4\alpha)\tau e^{-\tau} + 2\alpha e^{-2\tau}\right)}{R^4},$$
 (5.13)

which allows (5.12) to be rewritten as

$$0 = -\nabla \mathbf{P}^{(1)} + \mathcal{L}\left(\nabla^2 \mathbf{U}^{(1)}\right). \tag{5.14}$$

In addition to the usual no-slip and far-field boundary conditions, we anticipate that the free-surface boundary conditions at the interface are particularly crucial for this first-order solution. We substitute (5.11) into the first-order normal stress boundary condition (3.11b), and express the equations using the newly defined pressure variable, leading to the result

$$-\mathbf{P}^{(1)}\Big|_{Z=0} \boldsymbol{e}_z + 2\mathcal{L}\left(\boldsymbol{e}_z \cdot \boldsymbol{E}^{(1)}\Big|_{Z=0}\right) = \left(\frac{2\beta_p \left(1 - 2\alpha - \mathbf{e}^{-\tau} - (1 - 4\alpha)\tau \mathbf{e}^{-\tau} + 2\alpha \mathbf{e}^{-2\tau}\right)}{R^4}\right) - G\left(H^{(2)} - \frac{1}{BR}\frac{\partial}{\partial R}\left(R\frac{\partial H^{(2)}}{\partial R}\right)\right)\right) \boldsymbol{e}_z. \tag{5.15}$$

On the other hand, recall from (3.8) that  $H = O(Wi^2)$ . This implies that when T = O(Wi), we have  $(\partial H/\partial T) = O(Wi)$ . In other words, temporal variations in the interface shape will emerge in this first-order solution. Unlike for the steady interface shape (4.3), the corresponding kinematic boundary condition (2.15d) at this order becomes

$$U_Z^{(1)}\big|_{Z=0} = \frac{\partial H^{(2)}}{\partial \tau}.$$
 (5.16)

It is difficult to obtain exact analytical expressions for the velocity field that satisfies (5.14), (5.15) and (5.16) for arbitrary values of G = O(1). However, when  $G \gg 1$ , the method of dominant balance enables progress in determining the interface shape, with the dominant terms in this limit being the terms on the right-hand side of (5.15),

$$H_{transient}^{(2)}(R,\tau) \sim \left(\frac{1 - 2\alpha - e^{-\tau} - (1 - 4\alpha)\tau e^{-\tau} + 2\alpha e^{-2\tau}}{1 - 2\alpha}\right) H_{steady}^{(2)}(R) = O\left(G^{-1}\right),$$
(5.17)

with  $H_{steady}^{(2)}(R)$  given in (4.13). Note that (5.17) is regular at  $\alpha=1/2$  because the steady-state solution (4.13) is also proportional to  $1-2\alpha$ . To confirm the consistency of this dominant balance, we need to assess the relative magnitudes of the pressure and velocities in terms of the parameter G. From (5.17), the kinematic boundary condition (5.16) implies that  $U_Z^{(1)}=O(G^{-1})$ . According to the continuity equation (2.14a),  $U_R^{(1)}$  must match the order of  $U_Z^{(1)}$ , giving  $U^{(1)}=O(G^{-1})$ . This, in turn, implies from the momentum equation (5.14) that  $P^{(1)}$  is also of order  $O(G^{-1})$ . Consequently, both the pressure and the rate of strain on the left-hand side of (5.15) are of order  $O(G^{-1})$ , while the right-hand

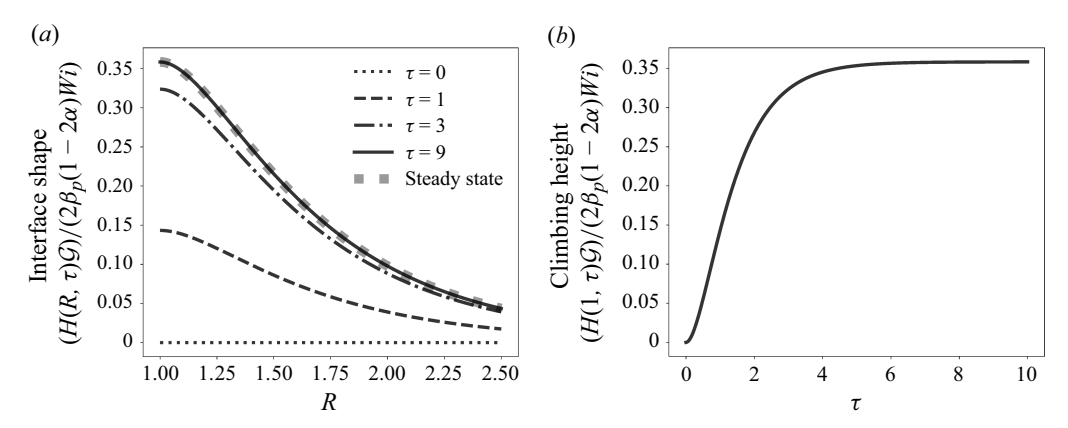


Figure 3. Time-varying interface shape for a Giesekus fluid. (a) Time evolution of the interface shape around an infinitely long rotating rod in a Giesekus fluid, with inertial effects absent, shown at times  $\tau = 0, 1, 3, 10$ . (b) Time evolution of the climbing height of a Giesekus fluid on the rotating rod, with inertial effects absent, evaluated at R = 1. All calculations were performed using B = 5 and  $\alpha = 0.25$ .

side remains of order O(1). Therefore, as  $G \gg 1$ , so that  $G^{-1} \ll 1$ , we conclude that the right-hand side forms a consistent dominant balance as desired. In § 4, we have derived a steady interface shape (4.13) for T = O(1), whereas in this section, we obtain a transient interface shape (5.17) for T = O(Wi). We note that

$$\lim_{\tau \to \infty} H_{transient}(R, \tau) = H_{steady}(R), \tag{5.18}$$

thus confirming that the interface dynamics occurs on a short time scale, with T = O(Wi), and that the transient interface shape approaches the steady interface shape at long times.

Figure 3(a,b) show the time evolutions of the scaled interface shape  $H(R,\tau)\mathcal{G}/[2\beta_p(1-2\alpha)Wi]$  and the scaled climbing height of a Giesekus fluid on the rotating rod,  $H(R=1,\tau)\mathcal{G}/[2\beta_p(1-2\alpha)Wi]$ , given in (5.17), with B=5 and  $\alpha=0.25$ . We observe that the transient interface height reaches a steady state at  $\tau\approx 6$ , with the interface shape becoming nearly flat for  $R\gtrsim 3$ .

### 6. Inclusion of small but finite inertial effects

# 6.1. Leading-order solution

As derived in § 5, the transient interface shape (5.17) remains positive, owing to the hoop stress in the viscoelastic fluids, which drives the fluid radially inwards and is responsible for rod climbing. However, introducing a small inertial effect may change the dynamics, as the resulting centrifugal force would push the fluid radially outwards. This competition between forces leads us to investigate how finite, small inertia may impact the interface height when both effects are present. In this section, we continue to use the stretched time scale  $\tau$  to examine the transient interface dynamics.

Incorporating inertial effects into our analysis, the momentum equation (2.17) is

$$Re\left(\frac{1}{Wi}\frac{\partial U}{\partial \tau} + U \cdot \nabla U\right) = \nabla \cdot \Sigma. \tag{6.1}$$

Rather than focusing our analysis on the Reynolds number, we find it more useful to base our analysis on the elasticity number El, which represents the ratio of elastic stress to

inertial stress (Denn & Porteous 1971):

$$El = \frac{Wi}{Re}. (6.2)$$

Consequently, the momentum equation (6.1) can be expressed as

$$El^{-1}\left(\frac{\partial U}{\partial \tau} + WiU \cdot \nabla U\right) = \nabla \cdot \Sigma. \tag{6.3}$$

Previously, we derived the interface shape for  $El \to \infty$ , and now aim to extend our analysis to cases where El is large. To isolate the nonlinear term  $U \cdot \nabla U$  from the leading-order velocity profile, we assume that El is at least O(1), indicating small but finite inertial effects with  $Re \lesssim Wi$ . When El is finite, the time-derivative  $\partial U/\partial \tau$  of the velocity field reappears, in contrast to the low-Reynolds-number approximation in §§ 4 and 5. To ensure that the problem is well-posed, we specify the velocity field at the initial time:

$$\boldsymbol{U} = \boldsymbol{0} \quad \text{at} \quad \tau = 0. \tag{6.4}$$

Besides the additional terms on the left-hand side of the momentum equation (6.3) and the new initial condition (6.4), the remaining constitutive equations and boundary conditions are identical to those in § 5. Specifically, the leading-order polymeric stress  $\Sigma_p^{(0)}$  can be expressed in terms of the leading-order rate-of-strain tensor, as shown in (5.3). This expression, combined with the momentum equation (6.3), allows us to derive the differential equation for the leading-order velocity field:

$$El^{-1}\frac{\partial \boldsymbol{U}^{(0)}}{\partial \tau} = -\nabla \mathcal{P}^{(0)} + \mathcal{L}\left(\nabla^2 \boldsymbol{U}^{(0)}\right). \tag{6.5}$$

Following the approach in § 5.1, we seek a solution where the leading-order interface is flat. Using the same reasoning, we deduce that  $\mathcal{P}^{(0)}=0$  and the velocity field is purely azimuthal,  $U^{(0)}=U^{(0)}(R,\tau)\,e_{\theta}$ . This allows us to reduce the vector differential equation (6.5) to a partial differential equation for an unknown scalar variable:

$$El^{-1} \frac{\partial U^{(0)}}{\partial \tau} = \mathcal{L} \left( \frac{1}{R} \frac{\partial}{\partial R} \left( R \frac{\partial U^{(0)}}{\partial R} \right) - \frac{U^{(0)}}{R^2} \right). \tag{6.6}$$

Equation (6.6) is formulated on the semi-infinite domain  $R \in [1, \infty)$  subject to the noslip boundary condition (2.15*a*), the far-field boundary condition (2.15*e*), and the initial condition (6.4), i.e.

$$U^{(0)}(1,\tau) = 1, \quad U^{(0)}(\infty,\tau) = 0, \quad U^{(0)}(R,0) = 0.$$
 (6.7)

Since the vortex solution 1/R represents the steady-state solution of (6.6) along with the specified no-slip and far-field boundary conditions, we decompose  $U^{(0)}$  into a steady-state component and a transient component:

$$U^{(0)}(R,\tau) = \frac{1}{R} + \tilde{U}^{(0)}(R,\tau). \tag{6.8}$$

As (6.6) is linear,  $\tilde{U}^{(0)}$  also satisfies (6.6) but with homogeneous spatial boundary conditions:

$$\tilde{U}^{(0)}(1,\tau) = 0, \quad \tilde{U}^{(0)}(\infty,\tau) = 0, \quad \tilde{U}^{(0)}(R,0) = -\frac{1}{R}.$$
 (6.9)

We approach this problem using a Weber transform W of order one (Watson 1966; Piessens 2000), an analogue of the Hankel transform on the semi-infinite domain  $[1, \infty)$ ,

by introducing

$$V[\tau;k] = \mathcal{W}\{\tilde{U}^{(0)}(R,\tau)\} = \int_{1}^{\infty} R \,\tilde{U}^{(0)}(R,\tau) \,Z_{1}(k,R) \,\mathrm{d}R, \tag{6.10}$$

with the kernel  $Z_1(k, R)$  given by

$$Z_1(k, R) = J_1(kR) Y_1(k) - Y_1(kR) J_1(k),$$
(6.11)

where  $J_1$  and  $Y_1$  are the first- and second-kind Bessel functions of order one, respectively. This transformation enables us to simplify the Bessel differential operator of order one acting on  $\tilde{U}^{(0)}$  on the right-hand side of (6.6), provided that  $\tilde{U}^{(0)}$  decays to zero at infinity:

$$W\left\{\frac{1}{R}\frac{\partial}{\partial R}\left(R\frac{\partial \tilde{U}^{(0)}}{\partial R}\right) - \frac{\tilde{U}^{(0)}}{R^2}\right\} = -k^2W\left\{\tilde{U}^{(0)}(R,\tau)\right\} - \frac{2}{\pi}\tilde{U}^{(0)}(1,\tau) = -k^2V[\tau;k]. \tag{6.12}$$

Note that the operator W acts on the R variable, while  $\mathcal{L}$  acts on  $\tau$ , which implies that the two operators commute:  $W \circ \mathcal{L} = \mathcal{L} \circ W$ . We apply the Weber transform to (6.6), yielding

$$El^{-1} \frac{\partial V[\tau; k]}{\partial \tau} = -k^2 \mathcal{L} \left( V[\tau; k] \right) = -k^2 \left( \beta_s V[t; k] + \beta_p e^{-\tau} \int_0^{\tau} V[s; k] e^s ds \right). \tag{6.13}$$

In this transformed variable, the initial condition becomes

$$V[0; k] = \mathcal{W}\left\{\tilde{U}^{(0)}(R, 0)\right\} = -\int_{1}^{\infty} Z_{1}(k, R) dR$$

$$= J_{1}(k) \int_{1}^{\infty} Y_{1}(kR) dR - Y_{1}(k) \int_{1}^{\infty} J_{1}(kR) dR$$

$$= \frac{1}{k} (J_{1}(k) Y_{0}(k) - J_{0}(k) Y_{1}(k)) = \frac{2}{\pi k^{2}},$$
(6.14)

where the last equality follows from the Wronskian of the zero-order Bessel differential equation. To solve (6.13), we first multiply both sides by  $e^{\tau}$  and then differentiate with respect to  $\tau$ , to obtain

$$El^{-1}\left(\frac{\partial^2 V}{\partial \tau^2} + \frac{\partial V}{\partial \tau}\right) = -k^2 \left(\beta_s \frac{\partial V}{\partial \tau} + V\right),\tag{6.15}$$

where we have used the relation  $\beta_s + \beta_p = 1$ . Equation (6.15) is a constant-coefficient second-order differential equation in time, which has solutions of the form

$$V[\tau; k] = C_1(k) e^{\lambda_+ \tau} + C_2(k) e^{\lambda_- \tau}, \qquad (6.16)$$

where  $\lambda_+$  and  $\lambda_-$  are roots of the equations

$$\lambda^{2} + \left(1 + k^{2} E l \beta_{s}\right) \lambda + k^{2} E l = 0.$$
 (6.17)

In particular,

$$\lambda_{\pm} = \frac{-1 - k^2 E l \beta_s \pm \sqrt{(1 + k^2 E l \beta_s)^2 - 4k^2 E l}}{2}.$$
 (6.18)

Although  $\lambda_{\pm}$  can be complex depending on the value of k, their real parts are always negative, except at k = 0, where one root is zero and the other is -1. In addition to the

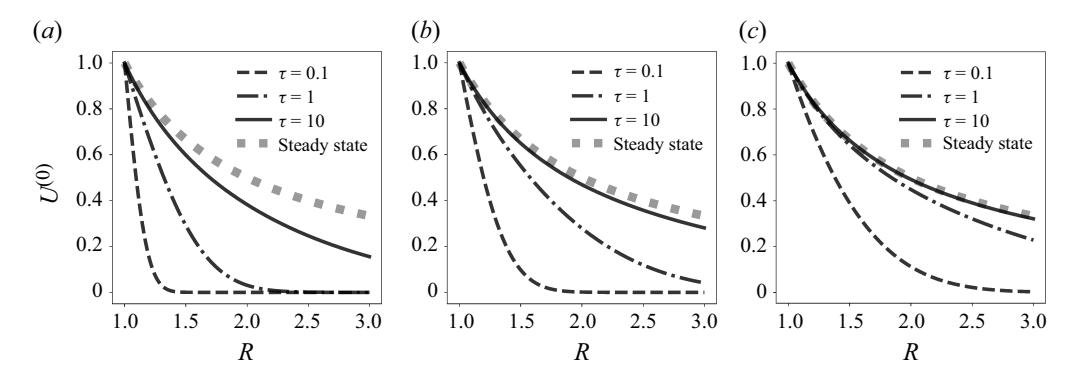


Figure 4. Time evolution of the leading-order velocity field  $U^{(0)}(R,\tau)$  around an infinitely long rotating rod in a Giesekus fluid, incorporating small but finite inertial effects, shown at times  $\tau=0.1,1,10$ , for (a) El=0.2, (b) El=1, and (c) El=5. All calculations were performed using  $\beta_p=0.5$ .

initial condition (6.14), evaluating (6.13) at  $\tau = 0$  provides an initial condition for  $\partial V / \partial \tau$ :

$$\frac{\partial V}{\partial \tau}[0;k] = -k^2 E l \beta_s V[0;k] = -\frac{2E l \beta_s}{\pi}.$$
(6.19)

Using (6.14), (6.16) and (6.19), and simplifying with (6.17), we find

$$V[\tau; k] = \frac{2}{\pi} \left( \frac{(1 + \lambda_{+}) e^{\lambda_{+} \tau} - (1 + \lambda_{-}) e^{\lambda_{-} \tau}}{k^{2} (\lambda_{+} - \lambda_{-})} \right), \tag{6.20}$$

where  $\lambda_+$  and  $\lambda_-$  are functions of k, El and  $\beta_s$ . Finally, we take an inverse Weber transform to obtain

$$\tilde{U}^{(0)}(R,\tau) = \int_0^\infty \frac{k V[\tau; k] Z_1(k, R)}{J_1^2(k) + Y_1^2(k)} dk 
= \frac{2}{\pi} \int_0^\infty \frac{\left( (1 + \lambda_+) e^{\lambda_+ \tau} - (1 + \lambda_-) e^{\lambda_- \tau} \right) Z_1(k, R)}{k(\lambda_+ - \lambda_-) \left( J_1^2(k) + Y_1^2(k) \right)} dk.$$
(6.21)

Although proceeding with (6.21) analytically is difficult, it is straightforward to handle numerically. In figure 4, we show the time evolution of the leading-order velocity profile  $U^{(0)}(R,\tau)$  for various values of El. We observe that larger El leads to a faster approach to a steady state in the transient velocity profile. Intuitively, when El is large, the elastic effect (Wi) is larger than the inertial effect (Re). A larger viscoelasticity accelerates the flow's return to equilibrium by emphasising the elastic 'spring-like' properties over inertial resistance, thus pushing the flow to a steady state faster.

### 6.2. First-order correction solution

In §§ 4.2 and 5.2, we used the leading-order velocity field  $U^{(0)}$  to calculate the polymeric force  $\nabla \cdot \Sigma_p^{(1)}$ , which is then incorporated into the pressure gradient  $\nabla \mathcal{P}^{(1)}$  to determine the transient interface shape. However, the leading-order velocity field (6.21) is challenging to work with directly. To address this, we first express  $\nabla \cdot \Sigma_p^{(1)}$  in terms of  $U^{(0)}$ , calculate the interface shape, and then transition to numerical computations as a final step. We find (see Appendix B for more detailed calculations)

$$\nabla \cdot \boldsymbol{\Sigma}_{p}^{(1)} = \beta_{p} e^{-\tau} \int_{0}^{\tau} \nabla^{2} \boldsymbol{U}^{(1)} e^{s} ds - f(\boldsymbol{R}, \tau) \boldsymbol{e}_{r}, \qquad (6.22)$$

where

$$f(R,\tau) = 2\beta_p e^{-\tau} \int_0^{\tau} R \frac{\partial}{\partial R} \left( \frac{U^{(0)}}{R} \right) \left( \int_0^S \frac{\partial}{\partial R} \left( \frac{U^{(0)}}{R} \right) e^s \, ds \right) dS$$
$$+ \alpha \beta_p e^{-\tau} \frac{\partial}{\partial R} \left( \int_0^{\tau} e^{-S} R^2 \left( \int_0^S \frac{\partial}{\partial R} \left( \frac{U^{(0)}}{R} \right) e^s \, ds \right)^2 dS \right). \tag{6.23}$$

At first order, the momentum equation (6.3) becomes

$$El^{-1}\left(\frac{\partial \boldsymbol{U}^{(1)}}{\partial \tau} + \boldsymbol{U}^{(0)} \cdot \nabla \boldsymbol{U}^{(0)}\right) = -\nabla \mathcal{P}^{(1)} + \beta_s \nabla^2 \boldsymbol{U}^{(1)} + \nabla \cdot \boldsymbol{\Sigma}_p^{(1)}. \tag{6.24}$$

The second term on the left-hand side of (6.24) represents the centrifugal force generated by the (start-up) vortex:

$$U^{(0)} \cdot \nabla U^{(0)} = -\frac{(U^{(0)})^2}{R} e_r. \tag{6.25}$$

Observe that both the centrifugal force (6.25) and the polymeric force induced by the leading-order flow (second term of (6.22)) are directed radially. To simplify, we introduce a modified pressure variable that combines these two conservative forces:

$$P^{(1)}(R,\tau) = \mathcal{P}^{(1)}(R,\tau) + \int_{R}^{\infty} \left( \frac{(U^{(0)}(s,\tau))^2}{El \, s} - f(s,\tau) \right) ds. \tag{6.26}$$

Combining (6.24) and (6.26) allows us to express the momentum equation as

$$El^{-1} \frac{\partial \boldsymbol{U}^{(1)}}{\partial \tau} = -\nabla \mathbf{P}^{(1)} + \mathcal{L}\left(\nabla^2 \boldsymbol{U}^{(1)}\right). \tag{6.27}$$

Following an argument similar to that in § 5.2, in the limit where  $G \gg 1$ , we argue through the dominant balance that the interface shapes are determined by the pressure contributions from the inertial and polymeric stresses in (6.26). We obtain a differential equation

$$H_{inertia}^{(2)} - \frac{1}{BR} \frac{\partial}{\partial R} \left( R \frac{\partial H_{inertia}^{(2)}}{\partial R} \right) = \frac{1}{G} \int_{R}^{\infty} \left( f(s, \tau) - \frac{(U^{(0)}(s, \tau))^2}{El \, s} \right) \mathrm{d}s := F(R, \tau). \tag{6.28}$$

The solution to this differential equation with the boundary conditions (2.15b) and (2.15e) is

$$H_{inertia}^{(2)}(R,\tau) = BI_1(\sqrt{B})K_1^{-1}(\sqrt{B})\left(\int_1^\infty s \ K_0(\sqrt{B}s)F(s,\tau) \,\mathrm{d}s\right)K_0(\sqrt{B}R)$$

$$+ BI_0(\sqrt{B}R)\int_R^\infty s \ K_0(\sqrt{B}s)F(s,\tau) \,\mathrm{d}s$$

$$+ BK_0(\sqrt{B}R)\int_1^R s \ I_0(\sqrt{B}s)F(s,\tau) \,\mathrm{d}s. \tag{6.29}$$

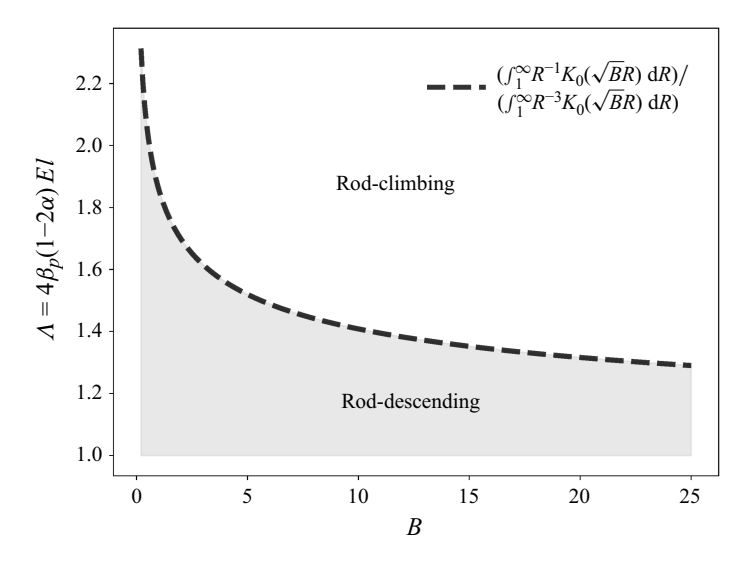


Figure 5. Phase diagram for the existence of the rod-climbing phenomenon around an infinitely long rotating rod in a Giesekus fluid, incorporating small but finite inertial effects. All calculations were performed in the range  $B \in (0.2, 25)$ .

Before we present numerical results to (6.29), we consider the steady interface shape in the presence of inertial effects. We substitute  $U^{(0)} \approx 1/R$  and let  $\tau \to \infty$  to find

$$F(R, \infty) = \frac{1}{G} \left( -\frac{1}{2ElR^2} + \frac{2\beta_p (1 - 2\alpha)}{R^4} \right). \tag{6.30}$$

The steady interface shape is readily obtained by substituting (6.30) into (6.29). At the rod (R = 1), the steady rise height can be simplified and is given by

$$H_{inertia}^{(2)}(1,\infty) = \frac{\sqrt{B}}{G} K_1^{-1}(\sqrt{B}) \left( -\frac{1}{2El} \int_1^\infty R^{-1} K_0(\sqrt{B}R) dR + 2\beta_p (1 - 2\alpha) \int_1^\infty R^{-3} K_0(\sqrt{B}R) dR \right).$$
(6.31)

Rod climbing, at the steady state, occurs when this rise height is positive, which corresponds to the criterion

$$\Lambda := 4\beta_p (1 - 2\alpha)El > \frac{\int_1^\infty R^{-1} K_0(\sqrt{B}R) dR}{\int_1^\infty R^{-3} K_0(\sqrt{B}R) dR}.$$
 (6.32)

Figure 5 illustrates a phase diagram as a function of the parameters  $\Lambda$  and B for the rodclimbing criterion (6.32). When B=O(1), the right-hand side of (6.32) takes a value approximately between 1 and 2, approaching 1 in the limit as  $B\to\infty$ . A necessary condition, but not sufficient, for the rod climbing at the steady state to occur, regardless of surface tension effects, is that  $\Lambda>1$ . For a given Bond number B, the climbing criterion (6.32) requires viscoelastic effects to surpass inertial effects for climbing to occur (represented by the elasticity number El), though the effective viscoelasticity is also reduced by the polymer solution's diluteness (represented by  $\beta_p$ ) and the polymer's chain mobility (represented by  $\alpha$ ). This highlights how the balance between viscoelasticity, inertia, polymer concentration and polymer mobility governs the climbing behaviour.

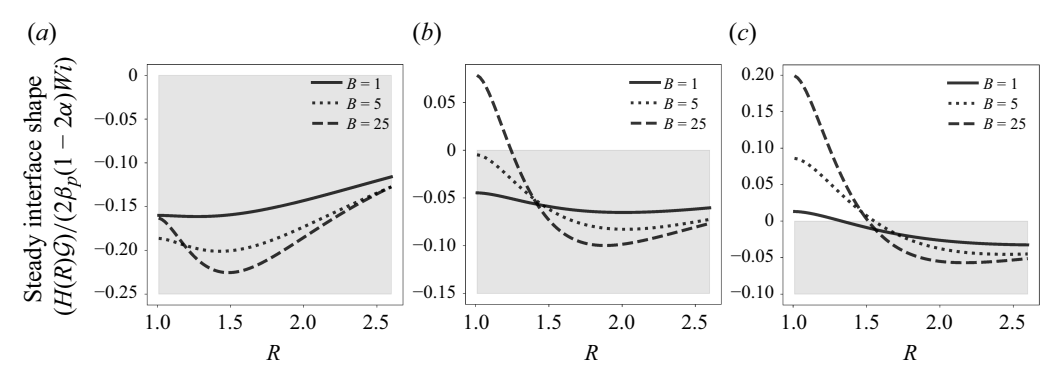


Figure 6. Steady-state interface shapes around an infinitely long rotating rod in a Giesekus fluid, incorporating small but finite inertial effects, for (a)  $\Lambda = 1$ , (b)  $\Lambda = 1.5$ , (c)  $\Lambda = 2$ , and Bond numbers B = 1, 5, 25.

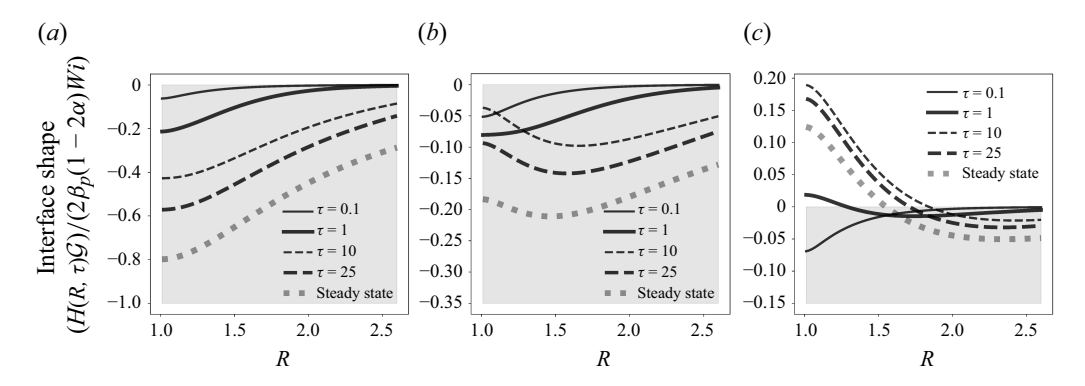


Figure 7. Time evolution of the transient interface shapes around an infinitely long rotating rod in a Giesekus fluid, incorporating small but finite inertial effects, shown at times  $\tau = 0.1$ , 1, 10, 25, for (a) El = 0.5, (b) El = 1, and (c) El = 2. All calculations were performed using  $\beta_p = 0.5$ ,  $\alpha = 0.25$  and B = 9.

Figure 6 shows the steady-state interface shape  $H_{inertia}(R, \infty)$  scaled by  $2\beta_p(1-2\alpha)Wi/\mathcal{G}$ , for various values of  $\Lambda$  and B. We consider three representative cases:  $\Lambda=1,1.5,2$ , which illustrate typical steady interface behaviours. For  $\Lambda=1$ , the interface height is negative when  $B\geqslant 1$ ; for  $\Lambda=2$ , it is positive in the same range. For  $\Lambda=1.5$ , the interface height may be either positive or negative depending on the Bond number: rod climbing occurs for  $B\gtrsim 5$ , but not for smaller values.

To examine the interface dynamics before reaching the steady state, we present the transient interface (6.29) obtained via numerical computations. In figures 7 and 8, we show the time evolution of the free surface (scaled by  $2\beta_p(1-2\alpha)Wi/\mathcal{G}$ ) for different elasticity numbers and Bond numbers. We observe that the impulsive motion of the rod initially causes a sudden dip in the fluid interface near the rod, an effect that is more pronounced at lower elasticity numbers due to stronger inertial forces. As time progresses, inertia continues to drive the interface downwards, while viscoelastic stresses act to push it upwards. When inertial effects outweigh viscoelastic effects, the interface height decreases monotonically until reaching a steady state, as illustrated for El = 0.5 in figure 7. At higher elasticity numbers, where viscoelastic effects are more dominant, the interface initially climbs due to the stronger viscoelastic response. However, because viscoelastic stresses

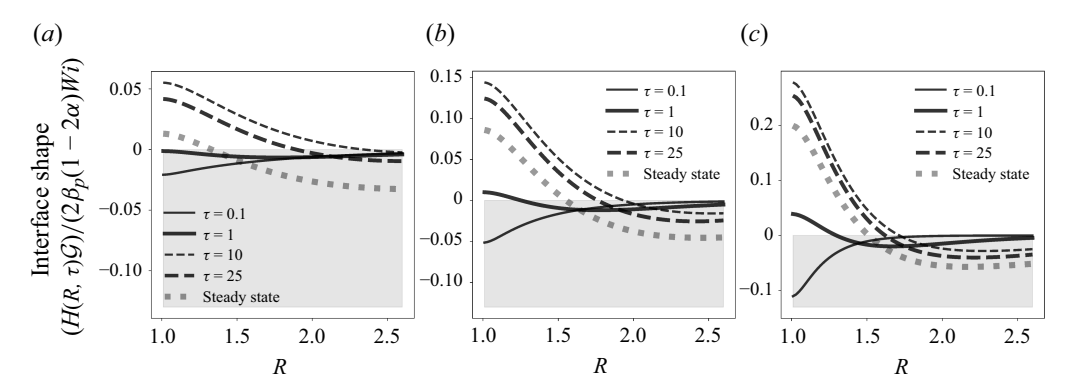


Figure 8. Time evolution of the transient interface shapes around an infinitely long rotating rod in a Giesekus fluid, incorporating small but finite inertial effects, shown at times  $\tau = 0.1$ , 1, 10, 25, for (a) B = 1, (b) B = 5, and (c) B = 25. All calculations were performed using  $\beta_p = 0.5$ ,  $\alpha = 0.25$  and El = 2.

relax faster than inertial effects, the climbing height eventually peaks and then decreases, governed by the slower relaxation of inertia towards its steady-state behaviour.

Depending on the spatial location of the interface, the viscoelastic fluid rises at varying rates due to the interplay between inertial and viscoelastic contributions. For El = 0.5, 1, 2, we observe that the interface shape exhibits non-monotonic behaviour primarily within the range  $1 \le R \le 1.5$ . At larger values of R, the interface deformation becomes smaller and more regular.

### 7. Conclusions

In this study, we explore the transient dynamics of the rod-climbing phenomenon, deriving the transient interface shape in the small-deformation regime for a Giesekus fluid. We show that normal stress differences drive the rod-climbing phenomenon, with the second normal stress difference reducing the climbing height, while the shear-thinning behaviour does not affect the leading-order rise. Our analysis emphasises the interplay between viscoelasticity, gravity and surface tension, characterised respectively by the Weissenberg number (Wi), the dimensionless gravity parameter ( $\mathcal{G}$ ), and the capillary number (Ca), and we find that the small-deformation scenario corresponds to cases where  $Wi \ll 1, \mathcal{G} \gg 1/Wi$ and  $Ca \mathcal{G} = O(1)$ . These conditions enable us to employ a perturbation expansion for the velocity field and the rise height in terms of Wi with the aid of the domain perturbation method. Even though surface tension has been included in our analysis, we have assumed the contact angle  $\varphi = \pi/2$  to focus on the dynamics of the viscoelastic rise in absence of the capillary rise. Approximately, our analysis provides a formula for the additional rise height beyond the capillary rise height when the contact angle is  $\varphi < \pi/2$ . In contrast, earlier work by Joseph & Fosdick (1973) developed expansions based on the (small) angular rotation speed  $\Omega$ ; see also More et al. (2023). From a theoretical point of view, this approach is less desirable since  $\Omega$  is a dimensional parameter, which complicates the distinction between limits arising from other variables, such as gravity, surface tension and inertia. Although our analysis is conducted specifically with the Giesekus model, the approach can be applied to other viscoelastic models that exhibit a non-singular asymptotic structure in viscometric flows in the limit  $Wi \ll 1$ .

Most experiments on the rod-climbing phenomenon focus on regimes where fluids rise higher than predicted in this study, and form a thin film near the rod, deviating from the small-deformation scenario. One potential research direction to better understand this

behaviour is to analyse the phenomenon in the high-Weissenberg-number limit ( $Wi \gg 1$ ), as significant climbing heights are observed at high angular velocities. Recent studies (Boyko, Hinch & Stone 2024; Hinch et al. 2024) have investigated Oldroyd-B fluid flows in narrow, slowly varying contractions under conditions similar to  $Wi \gg 1$ , using the ultradilute limit and curvilinear transformations to simplify the equations. However, extending these methods to the rod-climbing problem may present a challenge as the flow is not unidirectional. Expanding our results to this high-Weissenberg-number scenario will help to improve the alignment with experimental data, and enable more accurate rheological measurements using the rod-climbing phenomenon. Another possible research direction is to consider weak viscoelasticity ( $Wi \ll 1$ ) while incorporating moderate gravity effects (G < 1/Wi), potentially revealing another distinguished limit where analytical solutions may be possible using asymptotic methods.

The methods developed in § 5 to analyse the boundary layer in time and in § 6 to account for finite inertial effects are broadly applicable and not limited to the rod-climbing phenomenon. We anticipate that our approach for the Giesekus model will be valuable for studying a wider range of time-dependent problems, such as start-up flows in complex fluids. While most theoretical work on viscoelastic flows has focused on steady-state scenarios, our study provides researchers with a versatile set of tools to gain deeper insight into how suspended polymers, and other similar microstructural elements, respond to unsteady flow fields.

Acknowledgements. We thank I. Christov, G. McKinley and E. Yariv for helpful discussions.

**Funding.** E.B. acknowledges support by grant no. 2022688 from the US-Israel Binational Science Foundation. H.A.S. acknowledges support from grant no. CBET-2246791 from the US National Science Foundation.

Declaration of interests. The authors report no conflict of interest.

### Appendix A. Kernel of a linear operator $\mathcal{L}$

Here, we prove a proposition about the kernel of the linear operator  $\mathcal{L}$  used in § 5.1. Suppose that  $\mathcal{L}$  is a linear operator defined by

$$\mathcal{L}(\boldsymbol{F}(\boldsymbol{X},t)) = \beta_s \, \boldsymbol{F}(\boldsymbol{X},t) + \beta_p \, e^{-t} \int_0^t \boldsymbol{F}(\boldsymbol{X},s) \, e^s \, \mathrm{d}s. \tag{A1}$$

If  $\mathcal{L}(F(X,t)) = \mathbf{0}$  for all  $(X,t) \in \mathbb{R}^3 \times [0,\infty)$ , then  $F(X,t) = \mathbf{0}$  for all  $(X,t) \in \mathbb{R}^3 \times [0,\infty)$ .

The proof is as follows. Suppose that  $\mathcal{L}(F(X,t)) = \mathbf{0}$  for all  $X \in \mathbb{R}^3$  and  $t \ge 0$ . Evaluating the equation at t = 0, the second term on the right-hand side of (A1) vanishes, leaving us with  $F(X,0) = \mathbf{0}$  as  $\beta_s \ne 0$ . We may now take a time derivative of the equation  $e^t \mathcal{L}(F(X,t)) = \mathbf{0}$  to obtain

$$\frac{\mathrm{d}}{\mathrm{d}t} \left( e^t \mathcal{L}(\boldsymbol{F}(\boldsymbol{X}, t)) \right) = \frac{\mathrm{d}}{\mathrm{d}t} \left( \beta_s \, \boldsymbol{F}(\boldsymbol{X}, t) \, e^t + \beta_p \int_0^t \boldsymbol{F}(\boldsymbol{X}, s) \, e^s \, \mathrm{d}s \right)$$

$$= \beta_s \frac{\mathrm{d}}{\mathrm{d}t} \left( \boldsymbol{F}(\boldsymbol{X}, t) \, e^t \right) + \beta_p \, \boldsymbol{F}(\boldsymbol{X}, t) \, e^t = \boldsymbol{0}. \tag{A2}$$

It follows that this first-order ordinary differential equation in terms of F(X, t) e<sup>t</sup> yields a solution of the form

$$F(X, t) e^t = F(X, 0) e^{-\beta_p t/\beta_s} = \mathbf{0} \implies F(X, t) = \mathbf{0} \text{ for all } X \in \mathbb{R}^3 \text{ and } t \in [0, \infty).$$
(A3)

# Appendix B. Evaluating the hoop stress

Here, we provide detailed calculations for the expression  $\nabla \cdot \Sigma_p^{(1)}$  in (6.22). We begin by noting that the leading-order velocity field takes the form  $U^{(0)} = U^{(0)}(R, \tau) e_{\theta}$ . This enables us to write down the rate-of-strain tensor associated with the leading-order velocity field:

$$\boldsymbol{E}^{(0)} = \frac{1}{2} \left( \frac{\partial U^{(0)}}{\partial R} - \frac{U^{(0)}}{R} \right) (\boldsymbol{e}_r \boldsymbol{e}_\theta + \boldsymbol{e}_\theta \boldsymbol{e}_r) = \frac{R}{2} \frac{\partial}{\partial R} \left( \frac{U^{(0)}}{R} \right) (\boldsymbol{e}_r \boldsymbol{e}_\theta + \boldsymbol{e}_\theta \boldsymbol{e}_r) . \tag{B1}$$

Using (5.3), we express the leading-order polymeric stress as

$$\boldsymbol{\Sigma}_{p}^{(0)} = \left(\beta_{p} e^{-\tau} R \int_{0}^{\tau} \frac{\partial}{\partial R} \left(\frac{U^{(0)}}{R}\right) e^{s} ds\right) (\boldsymbol{e}_{r} \boldsymbol{e}_{\theta} + \boldsymbol{e}_{\theta} \boldsymbol{e}_{r}). \tag{B2}$$

At first order, the evolution of the polymeric stress (5.2) is

$$\boldsymbol{\Sigma}_{p}^{(1)} + \frac{\partial \boldsymbol{\Sigma}_{p}^{(1)}}{\partial \tau} = -\boldsymbol{U}^{(0)} \cdot \boldsymbol{\nabla} \boldsymbol{\Sigma}_{p}^{(0)} + \boldsymbol{\Sigma}_{p}^{(0)} \cdot \boldsymbol{\nabla} \boldsymbol{U}^{(0)} + (\boldsymbol{\nabla} \boldsymbol{U}^{(0)})^{\mathrm{T}} \cdot \boldsymbol{\Sigma}_{p}^{(0)} - \frac{\alpha}{\beta_{p}} \boldsymbol{\Sigma}_{p}^{(0)} \cdot \boldsymbol{\Sigma}_{p}^{(0)} + 2\beta_{p} \boldsymbol{E}^{(1)}.$$
(B3)

Next, we calculate each term on the right-hand side of (B3). Since  $U^{(0)}$  is azimuthal, we derive

$$\boldsymbol{U}^{(0)} \cdot \nabla \boldsymbol{\Sigma}_{p}^{(0)} = \frac{U^{(0)}}{R} \frac{\partial \boldsymbol{\Sigma}_{p}^{(0)}}{\partial \theta} = \left( 2\beta_{p} e^{-\tau} U^{(0)} \int_{0}^{\tau} \frac{\partial}{\partial R} \left( \frac{U^{(0)}}{R} \right) e^{s} ds \right) (\boldsymbol{e}_{\theta} \boldsymbol{e}_{\theta} - \boldsymbol{e}_{r} \boldsymbol{e}_{r}) . \tag{B4}$$

On the other hand,

$$\boldsymbol{\Sigma}_{p}^{(0)} \cdot \boldsymbol{\nabla} \boldsymbol{U}^{(0)} + (\boldsymbol{\nabla} \boldsymbol{U}^{(0)})^{\mathrm{T}} \cdot \boldsymbol{\Sigma}_{p}^{(0)} = 2\beta_{p} e^{-\tau} R \left( \int_{0}^{\tau} \frac{\partial}{\partial R} \left( \frac{\boldsymbol{U}^{(0)}}{R} \right) e^{s} ds \right) \times \left( \frac{\partial \boldsymbol{U}^{(0)}}{\partial R} \boldsymbol{e}_{\theta} \boldsymbol{e}_{\theta} - \frac{\boldsymbol{U}^{(0)}}{R} \boldsymbol{e}_{r} \boldsymbol{e}_{r} \right)$$
(B5)

and

$$\frac{\alpha}{\beta_p} \boldsymbol{\Sigma}_p^{(0)} \cdot \boldsymbol{\Sigma}_p^{(0)} = \alpha \beta_p \, e^{-2\tau} \, R^2 \left( \int_0^\tau \frac{\partial}{\partial R} \left( \frac{U^{(0)}}{R} \right) e^s \, ds \right)^2 (\boldsymbol{e}_\theta \boldsymbol{e}_\theta + \boldsymbol{e}_r \boldsymbol{e}_r). \tag{B6}$$

Thus (B3) can now be rewritten as

$$\Sigma_{p}^{(1)} + \frac{\partial \Sigma_{p}^{(1)}}{\partial \tau} = 2\beta_{p} E^{(1)} + 2\beta_{p} e^{-\tau} R^{2} \frac{\partial}{\partial R} \left( \frac{U^{(0)}}{R} \right) \left( \int_{0}^{\tau} \frac{\partial}{\partial R} \left( \frac{U^{(0)}}{R} \right) e^{s} ds \right) \mathbf{e}_{\theta} \mathbf{e}_{\theta}$$
$$-\alpha\beta_{p} e^{-2\tau} R^{2} \left( \int_{0}^{\tau} \frac{\partial}{\partial R} \left( \frac{U^{(0)}}{R} \right) e^{s} ds \right)^{2} (\mathbf{e}_{\theta} \mathbf{e}_{\theta} + \mathbf{e}_{r} \mathbf{e}_{r}). \tag{B7}$$

Multiplying both sides of (B7) with  $e^{\tau}$  and then integrating with respect to  $\tau$ , we arrive at

$$e^{\tau} \boldsymbol{\Sigma}_{p}^{(1)} = 2\beta_{p} \int_{0}^{\tau} \boldsymbol{E}^{(1)} e^{s} ds + 2\beta_{p} R^{2} \int_{0}^{\tau} \frac{\partial}{\partial R} \left( \frac{U^{(0)}}{R} \right) \left( \int_{0}^{S} \frac{\partial}{\partial R} \left( \frac{U^{(0)}}{R} \right) e^{s} ds \right) dS \boldsymbol{e}_{\theta} \boldsymbol{e}_{\theta}$$
$$- \alpha \beta_{p} R^{2} \int_{0}^{\tau} e^{-S} \left( \int_{0}^{S} \frac{\partial}{\partial R} \left( \frac{U^{(0)}}{R} \right) e^{s} ds \right)^{2} dS \left( \boldsymbol{e}_{\theta} \boldsymbol{e}_{\theta} + \boldsymbol{e}_{r} \boldsymbol{e}_{r} \right). \tag{B8}$$

Thus we conclude that

$$\nabla \cdot \boldsymbol{\Sigma}_{p}^{(1)} = \beta_{p} e^{-\tau} \int_{0}^{\tau} \nabla^{2} \boldsymbol{U}^{(1)} e^{s} ds$$

$$-2\beta_{p} e^{-\tau} \int_{0}^{\tau} R \frac{\partial}{\partial R} \left( \frac{\boldsymbol{U}^{(0)}}{R} \right) \left( \int_{0}^{S} \frac{\partial}{\partial R} \left( \frac{\boldsymbol{U}^{(0)}}{R} \right) e^{s} ds \right) dS \boldsymbol{e}_{r}$$

$$-\alpha\beta_{p} e^{-\tau} \frac{\partial}{\partial R} \left( \int_{0}^{\tau} e^{-S} R^{2} \left( \int_{0}^{S} \frac{\partial}{\partial R} \left( \frac{\boldsymbol{U}^{(0)}}{R} \right) e^{s} ds \right)^{2} dS \right) \boldsymbol{e}_{r}.$$
(B9)

#### REFERENCES

BEAVERS, G.S. & JOSEPH, D.D. 1975 The rotating rod viscometer. J. Fluid Mech. 69 (3), 475-511.

BEAVERS, G.S., YOO, J.Y. & JOSEPH, D.D. 1980 The free surface on a liquid between cylinders rotating at different speeds. Part III. *Rheol. Acta* 19 (1), 19–31.

BIRD, R.B., ARMSTRONG, R.C. & HASSAGER, O. 1987 Dynamics of Polymeric Liquids, Volume 1: Fluid Mechanics, 2nd edn. John Wiley and Sons.

BOYKO, E., HINCH, J. & STONE, H.A. 2024 Flow of an Oldroyd-B fluid in a slowly varying contraction: theoretical results for arbitrary values of Deborah number in the ultra-dilute limit. *J. Fluid Mech.* **988**, A10.

CHOI, H.J. 1991 Relaxation time of polymer solutions from rod-climbing height. Korean J. Chem. Engng 8, 18–22.

CHOI, H.J. & KIM, H.J. 1992 Relaxation time of polymer solutions from rod-climbing height (part 2). Korean J. Chem. Engng 9, 74–82.

DENN, M.M. & PORTEOUS, K.C. 1971 Elastic effects in flow of viscoelastic liquids. *Chem. Engng J.* 2 (4), 280–286.

EWOLDT, R.H. & SAENGOW, C. 2022 Designing complex fluids. Annu. Rev. Fluid Mech. 54, 413-441.

GIESEKUS, H. 1961 Einige bemerkungen zum fließverhalten elasto-viskoser flüssigkeiten in stationären schichtströmungen. *Rheol. Acta* 1, 404–413.

GIESEKUS, H. 1982 A simple constitutive equation for polymer fluids based on the concept of deformation-dependent tensorial mobility. *J. Non-Newtonian Fluid Mech.* 11 (1–2), 69–109.

HINCH, J., BOYKO, E. & STONE, H.A. 2024 Fast flow of an Oldroyd-B model fluid through a narrow slowly varying contraction. J. Fluid Mech. 988, A11.

JAMES, D.F. 2009 Boger fluids. Annu. Rev. Fluid Mech. 41, 129-142.

JOSEPH, D.D., BEAVERS, G.S. & FOSDICK, R.L. 1973 The free surface on a liquid between cylinders rotating at different speeds, part II. Arch. Rat. Mech. Anal. 49 (5), 381–401.

JOSEPH, D.D. & FOSDICK, R.L. 1973 The free surface on a liquid between cylinders rotating at different speeds, part I. Arch. Rat. Mech. Anal. 49 (5), 321–380.

MORE, R.V., PATTERSON, R., PASHKOVSKI, E. & MCKINLEY, G.H. 2023 Rod-climbing rheometry revisited. Soft Matt. 19 (22), 4073–4087.

MOROZOV, A. & SPAGNOLIE, S.E. 2015 Introduction to complex fluids. In *Complex Fluids in Biological Systems* (ed. S.E. Spagnolie), pp. 3–52. Springer.

OLDROYD, J.G. 1950 On the formulation of rheological equations of state. *Proc. R. Soc. Lond. A* **200** (1063), 523–541.

OLDROYD, J.G. 1951 The motion of an elastico-viscous liquid contained between coaxial cylinders. I. Q. J. Mech. Appl. Maths 4 (3), 271–282.

PIESSENS, R. 2000 The Hankel transform. In *The Transforms and Applications Handbook*, 2nd edn (ed. A.D. Poularikas). CRC Press.

SERRIN, J. 1959 Poiseuille and Couette flow of non-Newtonian fluids. Z. Angew. Maths Mech. 39, 295–299.
SIGINER, A. 1984 Free surface on a simple fluid between rotating eccentric cylinders. Part I: Analytical solution. J. Non-Newtonian Fluid Mech. 15 (1), 93–108.

WATSON, G.N. 1966 A Treatise on the Theory of Bessel Functions. Cambridge University Press.

WEISSENBERG, K. 1947 A continuum theory of rheological phenomena. Nature 159, 310-311.

YOO, J., JOSEPH, D.D. & BEAVERS, G.S. 1979 Higher-order theory of the Weissenberg effect. *J. Fluid Mech.* 92 (3), 529–590.